QUANTIFICATION OF NUCLEATION DELAY IN A HYDROUS PERALUMINOUS GRANITIC MELT

by

Maude Bilodeau

Department of Earth and Planetary Sciences

McGill University, Montreal

April 2023

A thesis submitted to McGill University in partial fulfilment of the requirements of the degree of Master of Science

TABLE OF CONTENTS

LIST OF FIGURES

LIST OF TABLES

ABSTRACT

In this study, a modified model based on the classical nucleation theory (CNT) was applied to a hydrous peraluminous pegmatite composition and tested against crystallization experiments performed in order to further constrain the quantification of nucleation delay in felsic melts. Crystallization experiments were performed in a piston cylinder apparatus at 630 MPa and temperatures between 750 and 1000 °C for durations ranging from 0.3 to 211 hours. Experimental run products were investigated by scanning electron microscopy (SEM) paired with energy dispersive spectroscopy (EDS) analyses of both crystalline and quenched liquid phases, the results of which were compared to a theoretical nucleation delay model. These experiments produced corundum and sillimanite, showing good agreement (within a factor of 2) with the modelled nucleation delays for typical granitic crystallization temperatures. Quartz crystals and spherulites of sodic plagioclase also nucleated, and although more data is required to better constrain the nucleation curves, the experiments showed good agreement with the model. The theoretical nucleation delay model was also applied to feldspar and quartz nucleation delay data available in the literature and showed good to intermediate results. This study represents a stepping-stone in improving our understanding of quantification of nucleation delay, adding to a small but growing body of existing literature on the topic. Though further studies are required, this thesis shows promising results in the quantification of nucleation delay in felsic melts and demonstrates the potential of the model.

RÉSUMÉ

Dans cette étude, un modèle modifié basé sur la théorie classique de nucléation fut appliqué à une composition pegmatitique peralumineuse hydratée et comparé à des expériences de cristallisation afin d'améliorer les paramètres de quantification des retards de nucléation dans les systèmes felsiques. Les expériences de cristallisation furent effectuées dans un appareil de cylindre à piston à 630 MPa et soumises à des températures variant entre 750 et 1000 °C pour des durées variant entre 0.3 et 211 heures. Les produits de ces expériences furent par la suite analysés à l'aide d'un microscope électronique à balayage (MEB) combiné à des analyses de spectroscopie à rayons X à dispersion d'énergie (EDS) des cristaux formés et des phases liquides refroidies. Les résultats furent par la suite comparés au modèle théorique de retard de nucléation. Nos expériences ont produit des corindons et des sillimanites et coïncident, avec un facteur de 2, avec les retards de nucléation modélisés pour des températures typiques pour la cristallisation de systèmes granitiques. Des cristaux de quartz et des feldspaths riches en sodium et sous forme de sphérulites furent aussi nucléés et même si plus de données sont nécessaires afin de déterminer le niveau de succès du modèle théorique à de plus basses températures, les expériences qui comportent du quartz et des feldspaths coïncident bien avec les délais de nucléation modélisés. Notre modèle fut aussi appliqué à des données provenant de la littérature sur les systèmes felsiques afin de compléter nos expériences. La comparaison entre les retards de nucléation théorique et les données provenant de la littérature démontre des niveaux de succès variables. Cette étude s'inscrit dans un mouvement relativement récent d'études visant à améliorer nos connaissances et nos méthodes servant à quantifier les délais de nucléation. Même si plusieurs études sont encore nécessaires afin de parfaire nos connaissances, ce manuscrit présente des résultats prometteurs démontrant les possibilités quant à la quantification des retards de nucléation dans les systèmes felsiques.

La cristallisation d'une idée a besoin d'un plancher, d'un plafond et des murs pour prétendre faire partie du monde. Les artistes produisent des œuvres physiques. Et le passage d'une idée vers un objet a besoin d'un pont.

Marc Séguin, L'atelier

REMERCIMENTS

Un énorme merci à Don. Merci pour ce mi-laboratoire, mi-garage, mi-atelier. Merci de m'avoir permis de patenter et de laisser libre cours à nos idées les plus saugrenues pour essayer de comprendre un peu mieux le minuscule. Merci pour toutes les discussions scientifiques (et non scientifiques) et de m'avoir demandé, à toutes nos rencontres hebdomadaires, « how can I help? ». Ce fut un privilège et un plaisir de travailler avec vous.

Merci à Lang pour l'aide précieuse lors de l'analyse des données au SEM, à Kristy et à Anne pour m'avoir permis de survivre au casse-tête administratif McGillois et à Jeanne et Bill d'avoir participer à mon comité d'évaluation et pour les discussions enrichissantes.

Merci à Monika de m'avoir fait confiance dès le début, merci à Catherine pour tous les bons conseils et ce, peu importe le contexte et merci à Raven d'avoir été très clairement la meilleure partenaire de maîtrise que j'aurais pu espérer. Vous continuez de m'impressionner et je me sens si chanceuse d'avoir pu évoluer et apprendre à vos côtés.

Merci aux colocs et à Erin, Em, Aube, Isa, et Dan pour votre douceur et votre écoute. Merci à maman, papa et Félix pour absolument tout. Merci de m'avoir écouté parler passionnément du tableau périodique. Merci de ne jamais m'avoir fait douter de votre support, même si ce que je faisais était un peu nébuleux. J'étais (je suis) une étudiante (une personne) plus équilibrée et heureuse grâce à vous tous.

INTRODUCTION

Nucleation is a key process in crystallization as it is the first step of crystal growth. Nucleation is defined as the formation of a nanoscopic, thermodynamically stable product phase, called the nucleus, resulting from the rearrangement of atoms (or molecules) initially present in a reactant phase (Kirkpatrick 1981, Fokin et al. 2006). Nucleation must occur for a crystal to grow to macroscopic sizes and impact the magma's properties. There is however a delay between the moment a phase becomes thermodynamically favoured and the actual start of nucleation, and this delay can vary from minutes to days depending on the systems and phases investigated (e.g., Gibb 1974; Fenn 1977; Swanson 1977; Donaldson 1979; Berkebile and Dowty 1982). Crystallization from melts, and more precisely, nucleation delay leading to crystallization, is investigated in this study.

Nucleation is highly dependent upon the degree of saturation of the nucleating phase. Supersaturation is a difficult property to measure and therefore undercooling (ΔT), which is the temperature below the liquidus temperature of a crystal in a melt, is often used as a proxy in nucleation studies. As the degree of undercooling increases, nucleation is facilitated, resulting in an increase of nucleation densities (Swanson 1977; Hammer 2008). Nucleation and undercooling have important impacts on rock textures, fabrics, and mineral shapes, and can also explain how magmas of similar compositions can generate rocks with very different textures and mineral assemblages when crystallized at the same pressure and temperature (Nabelek et al. 2010). An extreme example of this would be the contrast between rhyolitic obsidian, which is glassy, and granitic pegmatites, which can display meter-scaled crystals. The enigmatic process by which pegmatites form is thought to be partly associated with nucleation delay.

1. LITERATURE REVIEW

1.1 Pegmatites and their importance

Pegmatites are igneous rocks that are usually granitic in composition and enriched in fluxing components, the most common being H_2O, B and F, but also P, Cl, CO_2, S, Li, Rb, Cs, Be and rare earth elements (REEs) (Černý 1991; London 2005; Simmons and Webber 2008; Nabelek et al. 2010). This enrichment in minor elements and the progressive crystallization of pegmatitic bodies can result in the formation of exotic minerals such as beryl, spodumene, and tourmaline, which host critical metals that are of high importance in the fields of energy, transport, and telecommunication (Černý 1991; Linnen et al. 2012). However, most pegmatites remain compositionally near the haplogranite system, crystallizing mainly quartz and feldspar and lacking exotic minerals, miarolitic cavities, and hydrothermal envelopes (Černý 1991; London 2005). Nevertheless, simple pegmatites are also important for the glass, ceramics, and electronics industries (London 2018).

Since pegmatites are compositionally similar to ordinary, silicic igneous rocks, it is their texture that gives them their most defining features. Pegmatites are characterized by their large-scale crystals, up to meters in size, but more precisely, by the large range in crystal sizes often displayed in one outcrop, featuring crystals from the sub-millimetre to meter scale in close proximity, often only a metre or two from each other (Simmons and Webber 2008; London 2008). This characteristic contradicts the general understanding in geology where the timescale of crystallization is proportional to the size of the crystal. From cooling models based on pegmatitic dikes (e.g., Webber et al. 1999; London et al. 1999), it is known that pegmatites can crystallize very rapidly, on the timescale of days to months (London 2008, Nabelek et al. 2010), but if we

compare their sizes to the cooling history of typical volcanic and plutonic rocks, meter-sized crystals present in pegmatites should form on the scale of millions of years (London 2008).

Pegmatites are also characterized by their chemical heterogeneity on the macro- and microscopic scale. Heterogeneity is displayed through chemical zonation through the pegmatite body (Jahns and Burnham 1969; Simmons and Webber 2008; Maneta and Baker 2014; Sirbescu et al. 2023). Elements that are incompatible in quartz and feldspar concentrate in the residual melt, which results in their crystallization as rare minerals in the centre of the pegmatite (Jahns and Burnham 1969; London et al. 1989; Simmons and Webber 2008). The margins of zoned pegmatites are associated with small grain sizes, a complex mineral assemblage and granitic to aplitic textures, while the core is associated with large grain sizes, a monomineralic assemblage and coarse-grained pegmatitic textures (Černý 1991; Simmons and Webber 2008).

Pegmatites feature specific crystal morphologies and textures associated with varying degrees of undercooling, nucleation rates, and growth rates. Tabular and equant crystals are linked with low degrees of undercooling and low growth rates while skeletal, needle and dendritic crystals are linked with high degrees of undercooling, high growth rates and a small number of nucleation sites (London 2005, 2008; Simmons and Webber 2008). Distinctive pegmatitic textures, such as graphic intergrowths, wedge-shaped crystals, comb-like textures and radial arrangements are also associated with high degrees of undercooling (London 2005, 2008; Simmons and Webber 2008).

Most pegmatites are granitic in composition therefore, these types of melts have high viscosities, which first prevent nucleation in the melt by inhibiting diffusion, enabling the melt to intrude the host rock as a crystal-free liquid that may be supercooled (London 2005; Sirbescu et al. 2017). The presence of fluxes and volatiles then plays a vital role in the formation of pegmatitic

textures, even if the exact process by which they contribute to texture formation is still debated (e.g.: Jahns and Burnham 1969; London 2005, 2008; London and Morgan 2017). The presence of fluxes reduces the viscosity of the melt, increasing transport rates and allowing the melt to move rapidly and retain H_2O within the melt (Nabelek et al. 2010). This retention of H_2O lowers nucleation rates, leading the melt to start crystallizing further from its liquidus temperature (Nabelek et al. 2010; Simmons and Webber 2008). The presence of fluxes also increases diffusivity and crystal growth rates, producing a few number of large crystals (Jahns and Burnham 1969; Nabelek et al. 2010). The retention of fluxes and volatiles as the granitic melt is rapidly brought to high degrees of undercooling is the key to the formation of pegmatitic textures instead of equigranular granitic or rhyolitic ones (Nabelek et al. 2010).

1.2 Quantification of the classical nucleation theory (CNT) for calculation of nucleation delay

A first order phase transition theoretically occurs at a specific set of conditions, but in nature, that is not always the case. The rearrangement of atoms triggering a phase transition is a process arising from density, composition, concentration and other fluctuations randomly occurring within the initial phase (Kirkpatrick 1981; Kalikmanov 2013). These fluctuations generate a difference in chemical potentials between the initial and newly forming phase, making the phase transition thermodynamically favourable (Kalikmanov 2013). The nuclei must be larger than a certain size, called the critical size, in order to grow to macroscopic dimensions and be stable (Swanson 1977; Fokin et al. 2006). Moreover, for the nuclei to form and grow, elements must diffuse to the growing nuclei. But, nuclei do not form as soon as a new phase is thermodynamically stable in the melt; there is a delay before nucleation starts and steady-state rates of the new phase's growth are reached.

Nucleation can be defined as a homogeneous process, where nucleation has the same probability of occurring everywhere in the melt and is in contact solely with the parent phase, or as a heterogeneous process, where nucleation preferentially occurs on pre-existing phases (e.g., interfaces, already nucleated phases, etc.) (Kashchiev 2000; Fokin et al. 2006). Heterogeneous nucleation is usually associated with shorter nucleation delays as it is energetically more favourable to nucleate on pre-existing surfaces than directly from the melt. In general, this can be explained by the lower interfacial free energy between a pre-existing surface and a nucleus compared to the interfacial free energy between a nucleus and the melt from which it is growing (White 2013).

Classical nucleation theory (CNT) is based upon J. Willard Gibbs' (1875-1878) early work on the thermodynamic description of heterogeneous systems where the parent phase and the new nucleating phase are described as two homogeneous phases separated by a sharp planar interface of zero thickness; this is defined as homogeneous nucleation (Kirkpatrick 1981; Hammer 2004; Fokin et al. 2006). Assuming a spherical shape, the thermodynamic barrier for the formation of a nucleus can be described by

$$W^* = \frac{4}{3}\pi r^3 \Delta G_v + 4\pi r^2 \sigma \quad (1)$$

where W* is made up of two terms, namely the volume-free energy (the first term on the right-hand side) and surface-free energy (the second term on the right-hand side). The volume-free energy term describes the decrease of free energy of the system associated with the formation of a new crystalline phase while the surface-free energy term describes the increase in free energy due to the formation of an interface between the new and parent phase (De Yoreo and Vekilov 2003; Mazzotti et al. 2018). The volume-free energy contributes to the stabilization of a nucleus, whereas the interfacial free energy is a positive value and destabilizes the nucleus. At small radii, the

surface-free energy term dominates, and at this point, the nuclei will be unstable and tend to dissolve. At the critical radius size, the nuclei become large enough that the volume term dominates. At this size the interfacial free energy's impact on the total free energy of the system becomes minor and growth of the nucleus further decreases the total free energy of the system (De Yoreo and Vekilov 2003; Mazzotti et al. 2018). After reaching the critical nucleus size, the probability of decay is smaller than the probability of growth and the nuclei will be able to grow to macroscopic sizes (Kalikmanov 2013).

In order to form a thermodynamically stable nucleus the system must overcome a thermodynamic and a kinetic barrier, both of which can be described by the time lag before the onset of the steady state nucleation rate, which is the change from nucleation rate $I_{(t)}$ towards a steady-state rate, $I_{st,}$ which can be defined by:

$$I_{st} = I_0 \exp\left(\frac{-W^* + \Delta G_D}{k_B T}\right) \quad (2)$$

where I_{st} is the steady state nucleation rate, I_0 is a pre-exponential term depending on temperature, W^* is the change in Gibbs free energy associated with the formation of the critical cluster, i.e., the thermodynamic barrier, ΔG_D is the activation free energy required to transfer the structural units from the melt to the nucleus of the critical cluster size, i.e., the kinetic barrier, k_B is the Boltzmann constant, and T is the temperature (Turnbull and Fisher 1949; Kirkpatrick 1981; Fokin et al. 2006, 2008; Schmelzer 2008).

The following equation, from Fokin et al. (2006) and based on Kashichiev (1969), can be used to calculate the time lag before the onset of steady state ~~h~~omogeneous nucleation, referred to as the nucleation delay, τ:

$$\tau = \frac{16h}{\pi} \frac{\sigma}{\Delta G_v^2 a^4} exp \frac{\Delta G_D}{RT} \quad (3)$$

where h is Planck's constant, R is the gas constant, T is temperature (in Kelvin) and a is the size of a structural unit involved in the formation of the nucleus. Sigma, σ, is the interfacial free energy per unit area between the nucleus and the melt (De Yoreo and Vekilov 2003). ΔG_v is the bulk-free energy change per unit volume while G_D is the kinetic barrier, which can be expressed as the activation energy, Ea, required to transport structural units to the growing nucleus and represents the kinetic barriers to growth (e.g.: attachment processes, transport, rearrangement of bonds, etc.); this value must be overcome for the nuclei to grow (Hammer 2004). Multiple versions of equation 3 exist (e.g., Collins 1955; Kashchiev 1969; Slezov and Schmelzer 1999; etc.), varying by only 2 orders of magnitude in the value of the numerical constant (Gutzow and Schmelzer 1995).

Thus, for nucleation to occur, both a kinetic barrier and the surface-free energy associated with the crystal-liquid interface must be overcome by the system (Fokin et al. 2006, Hammer 2008). As the degree of undercooling increases, the size of the critical nuclei decreases, which facilitates nucleation. This decrease occurs up to the point where the critical nucleus size is smaller than one structural unit, removing the kinetic and thermodynamic barriers, and nucleation occurs as soon as fluctuations in the parent phase occur (Swanson 1977; De Yoreo and Vekilov 2003; Hammer 2008).

For heterogeneous nucleation, a correction is added to equation 3 due to the presence of a pre-existing surface that lowers the interfacial free energy, as indicated by the following equations from Fokin et al. (2006):

$$\tau_{het} = \tau \varphi^{\frac{1}{3}} \quad (4)$$

where

$$\varphi = \frac{1}{2} - \frac{3}{4}cos\theta + \frac{1}{4}cos^3\theta \quad (5)$$

and θ is the interior contact angle between the nucleation site and the nucleating phase (Fig. 1).

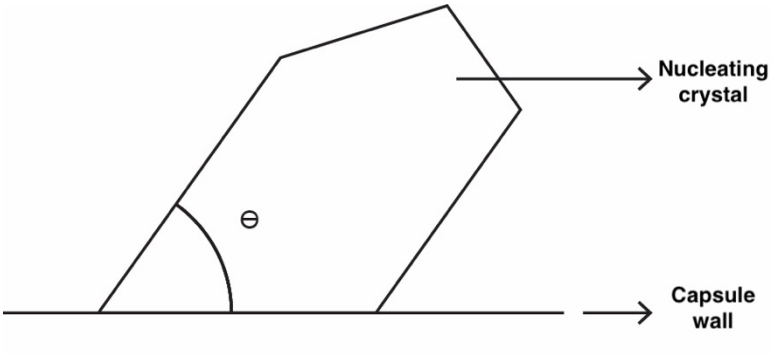

Figure 1: The interior contact angle (θ) is the angle between the nucleation site (here being the capsule wall) and the nucleating phase (here being the crystal).

1.3 Previous nucleation experiments in felsic melts

The concept of nucleation delay has been known since the beginning of the century, which also coincides with the beginning of experimental petrology, when Bowen (1913, as cited in London 2023) described plagioclase crystals forming well below their liquidus temperatures. Then, in the last 50 years, multiple attempts have been made to improve our understanding of crystallization in felsic melts through dynamic crystallization experiments (e.g., Fenn 1977; 1986; Maaløe and Wyllie 1975; Whitney 1975; Hammer 2004; Sirbescu et al. 2017; Rusiecka and Baker 2021). However, most of them focussed principally on the impact of water and the degree of undercooling on the crystallization sequence, texture formation, and growth rates rather than trying to quantify nucleation delay. Quantifying nucleation delay is of great importance because it can help better understand timescales of crystallization processes and help explain how melts of similar composition when subjected to similar temperatures and pressures can form drastically different rocks, e.g., obsidian, rhyolites and pegmatites. Having more quantifiable data on nucleation delay can also help constrain the timescale of volcanic eruptions and ascent rates.

A few more recent studies tried to quantitatively investigate nucleation delay (e.g.: Rusiecka et al. 2020; Devineau et al. 2020, etc.) and others also focussed on generating pegmatitic textures (e.g.: London 1989; Maneta and Baker 2014; Sirbescu et al. 2017; London and Morgan 2017; etc.), but more studies are still needed to construct a detailed method to quantify nucleation delay. To set this study in the framework of the field, we reviewed experiments studies providing quantifiable information on nucleation delay in felsic melts or studies for which it was possible to extract such data (Fig. 2).

Maaloe and Wyllie (1975) studied a natural composition of a peralkaline monzogranite from Norway at different water contents and degrees of undercooling between 900 and 705 °C for durations between 6 hours and 2 months, at 200 MPa. They observed plagioclase nucleating within 1 day at 875°C and biotite, within 2 days at 852°C. Alkali feldspar and quartz did not nucleate in runs of 60 days at temperatures close to the solidus.

Whitney (1975) performed crystallization experiments on a simplified hornblende-biotite granitic and granodiorite composition, under water-undersaturated and saturated conditions. He performed experiments principally at 200 and 800 MPa, at temperatures ranging between 625 and 1200 °C, durations varying between 3 and 33 days, and water contents varying between 0 and 20 wt%, with the goal of investigating the influence of composition, temperature and water content on the phase assemblage. He found plagioclase nucleating after 4 days at a lowest ΔT of -8 °C at 800 MPa and after 3 days at a ΔT of -37 °C at 200 MPa. Quartz nucleated after 4 days at ΔT of -24°C at 800 MPa and after 6 days at ΔT of -240°C at 200 MPa. He found that water content, pressure and composition have an important impact of the sequence and temperature of crystallization.

Fenn (1977) performed nucleation experiments on a synthetic haplogranitic composition between 950 °C and 500 °C for durations between 6 and 240 hours at 250 MPa and focussed primarily on growth rates, crystal morphologies and nucleation density of alkali feldspars. Fenn (1977) found that the nucleation delay for feldspar varied between 24 and 144 hours at a ΔT of -40°C, the delay being shorter for calcium-rich feldspar. In some instances of very high or very low degrees of undercooling experiments failed to nucleate any crystals after 72 hours or more. Nucleation delay varied with the composition of the feldspar crystals. The crystal morphology of feldspar varied with the degree of undercooling, with low degrees of undercooling associated with isolated tabular crystals and high degrees of undercooling with fine, closed spherulites, which is consistent with the observations of Lofgren (1974) in his study of plagioclase crystal morphology.

Swanson (1977) performed crystallization experiments on a simplified synthetic granite composition (in the $KalSi_3O_8$-$NaAlSi_3O_8$-$CaAl_2Si_2O_8$-SiO_2 system) under water-saturated and undersaturated conditions between 900 °C and 600 °C for durations between 24 and 144 hours at 800 MPa. He aimed to investigate nucleation density, growth rates, and crystal morphologies. He found nucleation delays varying between 24 and 144 hours and that the delay varied with the proximity to the liquidus temperature, i.e., the closer the crystallization temperature to the liquidus, the longer the delays, and with the bulk composition of the melt. Only granites with 3.5 wt% water or more were able to nucleate any crystals.

Evensen (2001) studied the impact of varying the physical state of the starting materials, i.e., glass rod, glass powder or a crystalline mixture, on textures, spatial relationships, nucleation delays and growth rates by performing crystallization experiments on a haplogranitic melt at 200 MPa. Evensen (2001) found that the nucleation delay decreased with increasing undercooling from

7 days at ΔT of -13 °C to 4.5 days at ΔT of -133°C, but the author didn't specify which phases nucleated and grew, although presumably they were feldspar and/or quartz.

Couch et al. (2003) performed crystallization experiments induced by decompression on a representative composition of the Soufrière Hills andesite at 875 °C between 160 and 30 MPa. They found nucleation delays between 1 and 4 hours for plagioclase at undercoolings between -38 and -151 °C. They found that the plagioclase crystal morphologies evolve with increasing degrees of undercooling from planar tabular, to hopper, swallowtail, and to dendritic and chain crystals at the highest degree of undercooling, which is in agreement with Lofgren (1974) and Hammer and Rutherford (2002).

London and Morgan (2017) performed crystallization experiments on the Macusani glass, a peraluminous S-type rhyolitic obsidian, and aimed to experimentally produce pegmatitic textures at 200 MPa between 575 and 450 °C over durations between 7 and 90 days. They were interested in varying their starting material between vesicular glass cores and glass powder (London 1989), and studying the impact of the degree of undercooling, duration and water content on percent crystallization. London and Morgan did not differentiate between the quartz and felspar nucleation delay and they found that the shortest nucleation delay for both phases was ~ 200 hours at a ΔT of -50 °C for 3 wt% water at 200 MPa.

Sirbescu et al. (2017) performed crystallization experiments with a synthetic peraluminous hydrous haplogranite composition that was enriched with boron and lithium at different degrees of undercooling and water concentrations at 300 MPa. Virgilite and stuffed quartz were the first phases to nucleate, with the shortest nucleation delay being 2 days at ΔTs of -10 and -20 °C. Alkali feldspar had the longest nucleation delay (minimum of 5 days at ΔT of -60 °C) and the lowest nucleation density of all the phases studied by Sirbescu et al. (2017). Quartz was present replacing

metastable stuffed quartz and virgilite after 30 days. Pegmatitic textures, namely skeletal, spherulitic and graphic textures, formed after a minimum of 14 days while low degrees of undercooling were associated with non-pegmatitic textures.

Devineau et al. (2020) performed equilibrium and dynamic crystallization experiments on a synthetic hydrous haplogranite composition at 200 MPa and were successful at nucleating alkali feldspar after 120 hours at a ΔT of -60 °C and quartz after 552 hours at a ΔT of -120°C. Alkali feldspar first appeared as tabular crystals, increasing in skeletal character as the degree of undercooling increased, while quartz displayed both anhedral and euhedral habits, regardless of the degree of undercooling or duration. Graphic textures of intergrown quartz and alkali feldspar were also observed, but only in the two longest experiments, 552 and 1440 hours, at a ΔT of - 120°C.

Arzilli et al. (2020) performed crystallization experiments to study the nucleation delay of alkali feldspar in peralkaline silicic melts under anhydrous, water-undersaturated, and water-saturated conditions, between 790 and 670 °C, for durations ranging from 0.5 to 420 hours, between 25 and 100 MPa. They found nucleation delays between 24 and 288 hours, the longest delay being associated with the smallest degree of undercooling and vice versa. The feldspars produced were highly skeletal, isolated crystals and no spherulitic textures were observed in their studies, which contrast other crystallization studies (e.g., Fenn 1977; Sirbescu et al. 2017; Rusiecka et al. 2020; etc.), who found feldspar forming spherulites within the same range of temperatures and durations as Arzilli et al. (2020), but at higher pressures.

Rusiecka et al. (2020) performed crystallization experiments on a hydrous metaluminous composition at temperatures ranging between 500 and 800 °C at 600 MPa. They found the shortest nucleation delay of 24 hours for quartz at a ΔT of -40 °C and for alkali feldspar of 24 hours at a

ΔT of -140 °C. The main objective of this paper was to present and evaluate an adjusted model based on the CNT to predict nucleation delays of quartz and alkali feldspar in felsic melts. The experiments and the modelled nucleation delay agreed within a factor of 5, demonstrating the potential to accurately constrain nucleation delay.

Rusiecka and Martel (2022) performed decompression-induced crystallization experiments on a hydrous, metaluminous rhyolite melt at temperatures ranging between 800 and 900 °C and pressures ranging between 25 and 200 MPa, converting their pressure data to degrees of undercooling values. Looking specifically at plagioclase nucleation, they found the shortest nucleation delay to be 30 hours at a ΔT of -50 °C. Skeletal morphologies are associated with this degree of undercooling, while euhedral and subhedral elongated morphologies are associated with lower degrees of undercooling (ΔT of -10°C). They showed that their experiments, in addition to those of Mollard et al. (2012), who performed similar experiments on another rhyolitic composition, agreed with the nucleation delay model elaborated by Rusiecka et al. (2020) within a factor of 2, demonstrating that undercooling produced from decompression yielded the same results as undercooling produced at isobaric conditions.

From this literature review, there is a lack of quantifiable nucleation delay data on natural granitic compositions and, more precisely, on common peraluminous granitic compositions (Fig. 2). This contribution will apply the Rusiecka et al. (2020) modified CNT model based on Fokin et al. (2006) to a natural hydrous peraluminous pegmatitic melt, comparing and evaluating this theoretical model against a series of crystallization experiments. Rusiecka et al.'s (2020) methodology and conditions (i.e. pressure and water content) were used to allow for a direct comparison with the study. The goal of this study was not to reproduce the natural mineralogy of the selected peraluminous composition and therefore, discussion of the natural rock was deemed

out of the scope of this research and is kept to a minimum. Most previous studies used haplogranite compositions to investigate the nucleation of feldspar and quartz (Fig. 2), but we are interested in how nucleation delay functions in a natural composition to further investigate how the addition of other cations into granitic melts affects their thermodynamic and kinetic properties (e.g., Swanson 1977; Whitney 1975; Naney and Swanson 1980). Studying nucleation delay in pegmatitic melts is of particular importance because, in addition to the degrees of undercooling, this parameter plays a key role in the formation of diagnostic pegmatite textures (London 2005). In addition, peraluminous melts, along with metaluminous melts, are the most common composition for pegmatites in nature, further justifying the focus of this research (Černý 1991).

This thesis reports timescales of nucleation for minerals of importance in peraluminous pegmatites and if the CNT model is able to accurately describe and predict nucleation delays over a range of felsic melt compositions. Our research on nucleation delay will improve the understanding of pegmatitic systems, providing quantitative and qualitative models describing the magmatic timescales and crystallization mechanisms responsible for their formation.

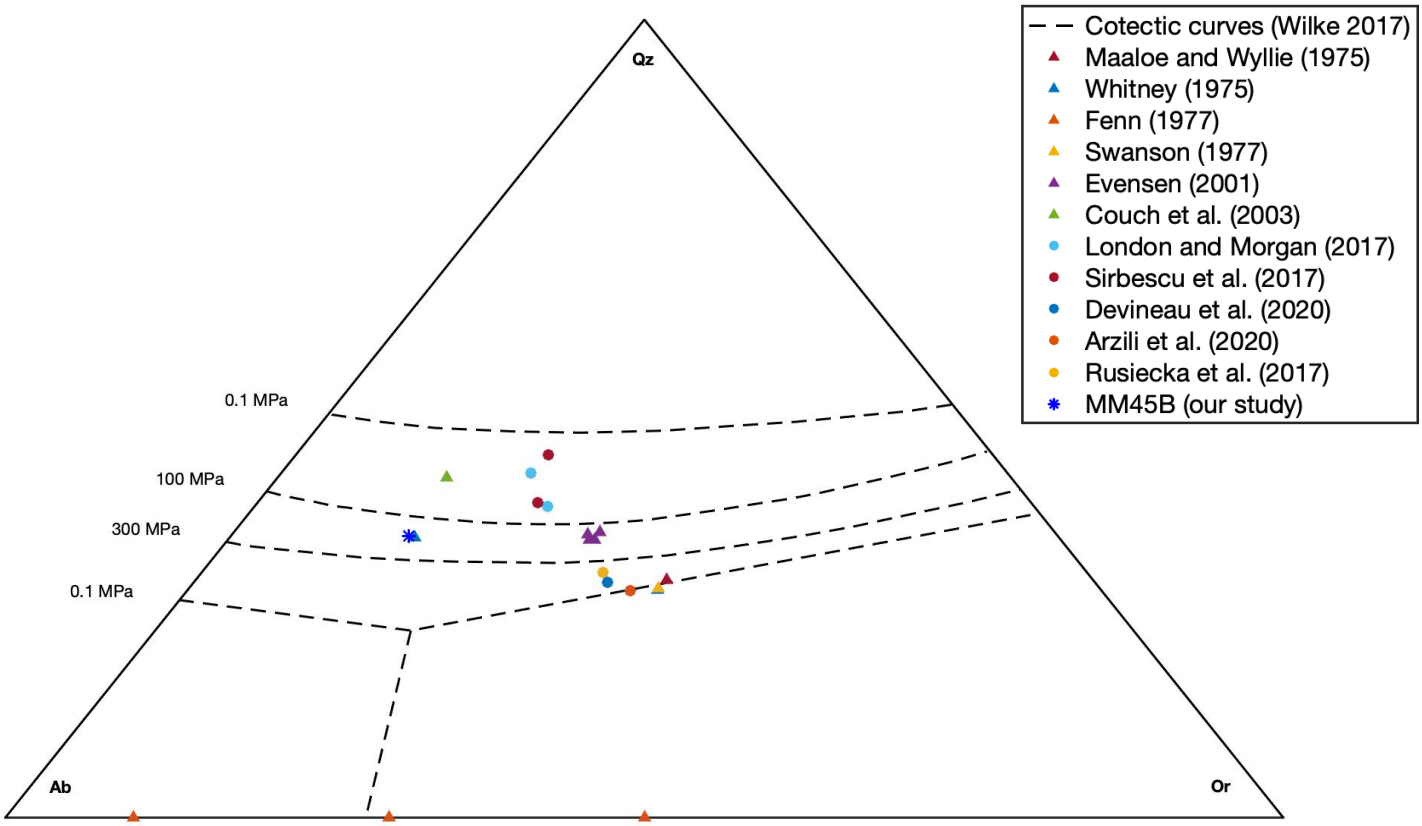

Figure 2: Comparative ternary diagram of the CIPW norm of felsic melts studied in quantitative studies on nucleation and crystallization summarized in this literary review. Filled symbols are the CIPW norm of studied melts and the dashed lines are the ternary projection of cotectic curves at various pressures as presented in Wilke (2017).

2. METHODOLOGY

2.1 Experimental Procedure

The aim of this study was to investigate nucleation delay in peraluminous granitic melts by studying the crystallization sequence of a natural pegmatite composition (with an alumina saturation index (ASI) of 1.45) from Mt. Mica, Oxford County, ME, USA (MM45B) (Simmons et al. 2016) under water undersaturated conditions (Table 1). Due to the heterogeneity of the Mt. Mica pegmatite, it was not possible to obtain a representative composition of the entire pegmatitic body from traditional whole rock analyses. The representative bulk chemical composition was therefore obtained by Simmons et al. (2016) by combining thorough mapping of the study area to estimate volumes of pegmatites and lepidolite pods and ICP-OES, ICP-MS and DCP analyses of 45 drill cores to obtain major and minor elements' concentrations. The elemental composition was then adjusted to match the mapped proportion of each mineral present.

Oxide	Wt%
SiO_2	72.08
TiO_2	0.07
Al_2O_3	17.33
FeOt	1.21
MnO	0.04
MgO	0.15
CaO	0.48
Na_2O	5.35
K_2O	2.08
P_2O_5	0.20
Li_2O	0.11
F	0.25
H_2O	1.16

Table 1. Bulk Composition of the Mt. Mica pegmatite (MM45B) in Simmons et al. (2016). The original table did not provide uncertainties of the oxide concentrations.

The MM45B glass powder used in the crystallization experiments was synthesized by melting rock powder in air at 1575 °C for 5 hours in a 1 atm furnace and subsequently grinding under ethanol, resulting in a crystal-free glass. Gold palladium ($Au_{75}Pd_{25}$) capsules of 2 mm in diameter and 8 mm in length were loaded with MM45B and 3.27 ± 0.07 wt% water, which adds to the initial water content of the Mt. Mica pegmatite of 1.16 wt%. In total, each capsule has 4.25 ± 0.07 wt% water. The capsules were welded in a water bath to prevent water loss. The capsules were then weighed and heated for at least an hour in an oven at 110 °C and weighed again to verify the absence of leaks. Experiments were performed in a piston-cylinder apparatus. The assembly was composed of crushible alumina pieces inside a graphite furnace, which was surrounded by a Pyrex sleeve, NaCl cylinders (salt cells) and a lead sheet (Fig. 3). Repeat experiments were performed at every run condition by placing two or three identical capsules into drilled holes in a crushable alumina piece. To minimize water loss and empty space between the alumina and the capsules, the holes were filled with alumina hydroxide powder. Temperatures were recorded using a tungsten rhenium (type C) thermocouple inserted in the middle of the assembly. Crystallization experiments were performed by heating the sample to 1100 °C at a rate of 100 °C/min while simultaneously increasing the pressure to 630 MPa. These pressure and temperature conditions were maintained for 24 hours to homogenize the melt composition. The homogenization temperature was chosen to be above the liquidus temperature to ensure the absence of crystals when starting the nucleation experiments. After this 24 h homogenization step the capsules were cooled at a rate of 30 °C/min to the desired crystallization temperature, which varied between 750 and 1000 °C, and remained at the chosen temperature for 0.5 to 211 hours. All experiments were isobarically quenched.

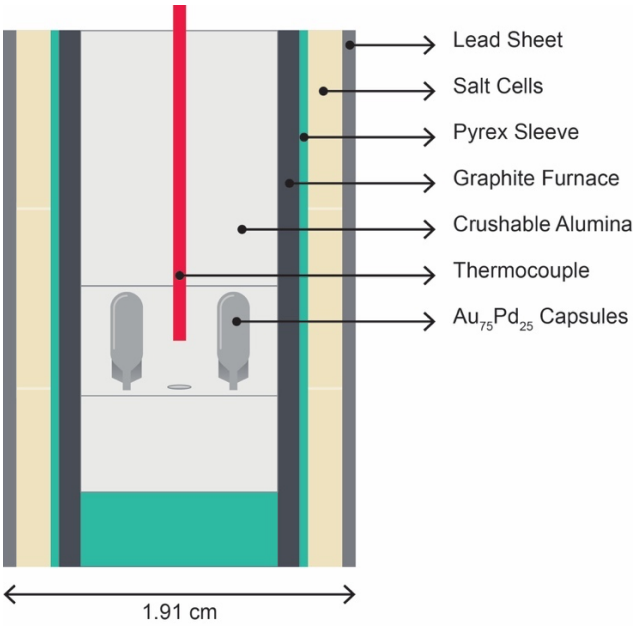

Figure 3 : Detailed cross-section of piston cylinder assembly used in this study.

2.2 Analytical Techniques

After each experiment the unopened experimental capsules were immersed in epoxy, ground, and polished. They were analyzed using a Hitachi SU5000 scanning electron microscope (SEM) at McGill University with an accelerating voltage of 15 kV to obtain backscattered-electron (BSE) images in order to characterize the run products formed in the experiments. Qualitative and quantitative analyses were performed using energy dispersive spectroscopy (EDS) to obtain the chemical compositions of the crystalline and glassy phases present in the samples. The semi-quantitative chemical composition data was collected using an Oxford Instruments SDD detector coupled with Aztec software. The EDS analyses of the quenched glass produced in experiments above the liquidus temperature agree with the published composition of the MM45B glass (Table 2), demonstrating the accuracy of this method of analysis. Measurements, annotations, and image alterations (i.e., increasing contrast and brightness) of the obtained BSE images were performed using ImageJ software (NIH Image; Abramoff et al., 2004; Schneider et al., 2012).

The water concentrations in glasses quenched from a few experiments were determined by Raman spectroscopy following the method of Behrens et al. (2006) and Fortin et al. (2015). Raman spectra were collected at McGill University using a Renishaw InVia confocal micro-Raman spectrometer with a 532 nm laser and 100X Leica microscope objective. The power was set to 10 % (50 mW), and a 2400 l/mm grating system with a 50 μm slit was used. The spectra were recorded using Wire 4.2 software. The acquisition time was set to 40 seconds and repeated 5 times. The spectra were quantified using a set of hydrous rhyolitic glass standards (Fortin et al., 2015).

Oxide	Wt% (Simmons et al. 2016)	Wt% (EDS analyses - our study)	Standard deviation on EDS analyses ($\boldsymbol{\sigma}$)
SiO_2	72.99	73.61	0.17
TiO_2	0.07	0.00	0.00
Al_2O_3	17.55	17.41	0.22
Fe_2O_3	1.19	1.06	0.06
MnO	0.04	0.26	0.02
MgO	0.16	0.13	0.04
CaO	0.48	0.50	0.02
Na_2O	5.42	5.03	0.11
K_2O	2.10	2.00	0.05

Table 2. Normalized MM45B composition to the 9 main oxides present in the Mt. Mica composition comparing Simmons et al. (2016) analyses with our EDS analyses of the quenched glass composition of MM45B at 1070°C for 96 hours. The standard deviation was calculated by the EDS software and was based on seven analyses. The table shows that the concentrations measured are in close agreement with each other, demonstrating the accuracy of the EDS analyses used in this study.

2.3 Determining the liquidus temperatures

Determining the bulk liquidus temperature of our composition is necessary to choose the homogenization temperature as it is important that no crystals are present in the melt before starting nucleation delay experiments. Melting experiments using the original crystalline rock powder were carried out prior to all other sets of experiments. The capsules and assemblies were made following the same procedure as for the nucleation experiments. Each assembly, placed into the piston cylinder apparatus, was brought directly to the desired temperature, which varied between 895 and 1070 °C, at a rate of 100 °C/min and remained at that temperature for 96 hours (4 days). After isobarically quenching the experiments, the capsules were opened, and the experimental run products were ground to make oil-immersion grain mounts. They were observed under petrographic microscope to verify the presence or absence of crystals. The presence of crystals in melting experiments at 1040 °C and the absence of crystals in the melting experiment at 1070 °C constrain the liquidus of MM45B with 4.25 wt% H_2O at 630 MPa to be of 1055 ±15 °C.

Melting experiments were also carried out to determine the specific liquidus of each crystallizing phases present in our nucleation experiments. This set of melting experiments was performed at temperatures at 850, 950 and 1000 °C, for durations of 110 and 115 hours. After being isobarically quenched, the experimental run products were analyzed following the same methodology as for the crystallization experiments. These experimental liquidus temperatures were compared to theoretical equilibrium liquidus temperatures calculated by the rhyolite MELTS thermodynamic modelling software (Ghiorso and Sack 1995; Gualda et al. 2012).

2.4 Modelling Nucleation: Modifying the Classical Nucleation Theory to consider the presence of a Diffuse Interface

Crystallization experiments performed on a hydrous peraluminous melt were compared to the nucleation curves of plagioclase, quartz, sillimanite and corundum, which we calculated using Equation 3 for homogeneous nucleation and Equation 4 for heterogeneous nucleation, depending of the dominant type of nucleation observed. The thermodynamic and kinetic data necessary for the calculation were obtained from the literature following the established techniques and derivations as fully described in Rusiecka (2020) and briefly discussed here.

The size of a structural unit, *a*, was set as the radius of Si^{4+} ions (0.26×10^{-10} m, Shannon 1976) for quartz, plagioclase and sillimanite following Rusiecka et al. (2020), while it was set as the radius of Al^{3+} ions (0.39×10^{-10} m, Shannon 1976) for corundum. The bulk-free energy change per unit volume ΔG_v, was calculated using the Gibbs free energy (ΔG) obtained using rhyolite MELTS (Ghiorso and Sack 1995; Gualda et al. 2012). The Gibbs free energy, which is a value given per mole, was converted to the bulk-free energy, which is the value given per unit volume, by using the molar volumes of the minerals (Rusiecka et al. 2020). The activation energy values used, E_a, were the silicon-aluminum interdiffusion activation energies measured by Baker (1990, 1992) in anhydrous and hydrous metaluminous rhyolitic melts of similar compositions to that of this study.

The CNT assumes a sharp planar interface between the growing nucleus and the melt, regardless the size of the nucleus, and that both the nucleating phase and the initial bulk phase have the same thermodynamic properties (Fig. 4A) (Gránásy 1993; Hammer 2004). These assumptions are thought to explain why CNT fails to accurately describe nucleation delay by several orders of magnitude in multiple systems (Gránásy 1996; Hammer 2004). To account for

this discrepancy, the CNT model used in this study was adjusted to qualitatively consider the diffuse interface theory (DIT) (Gránásy 1993). The DIT considers an interface between the nucleus and the melt with intermediate properties (i.e., enthalpy and entropy) between the two phases (Gránásy 1993). The solid nucleus has a structural influence on the melt interface, but that same interface has an atomic configuration more similar to that of a melt than a solid (Hammer 2004) (Fig. 4B). This interface is also size dependent (Gránásy 1993). In the DIT, the work of formation of the critical nucleus, the thermodynamic barrier (W, equation 1), is influenced by the entropy and enthalpy of the interface, as described by the following equation when considering a nucleating sphere:

$$W = \frac{4\pi}{3}\left(R_H^3 \Delta h_0 - R_S^3 T \Delta s_0\right) \quad (6)$$

With R_H and R_S being the position of the enthalpy and entropy surface, Δh_0 and Δs_0 being the values of the enthalpy and entropy per unit volume, respectively measured at the center of the nucleus (Gránásy 1993). Although, this equation was not considered in this study, which is why we state that the DIT was only qualitatively considered, we incorporated the concept of an interfacial region at the boundary between the nucleus and the melt in our nucleation delay calculations.

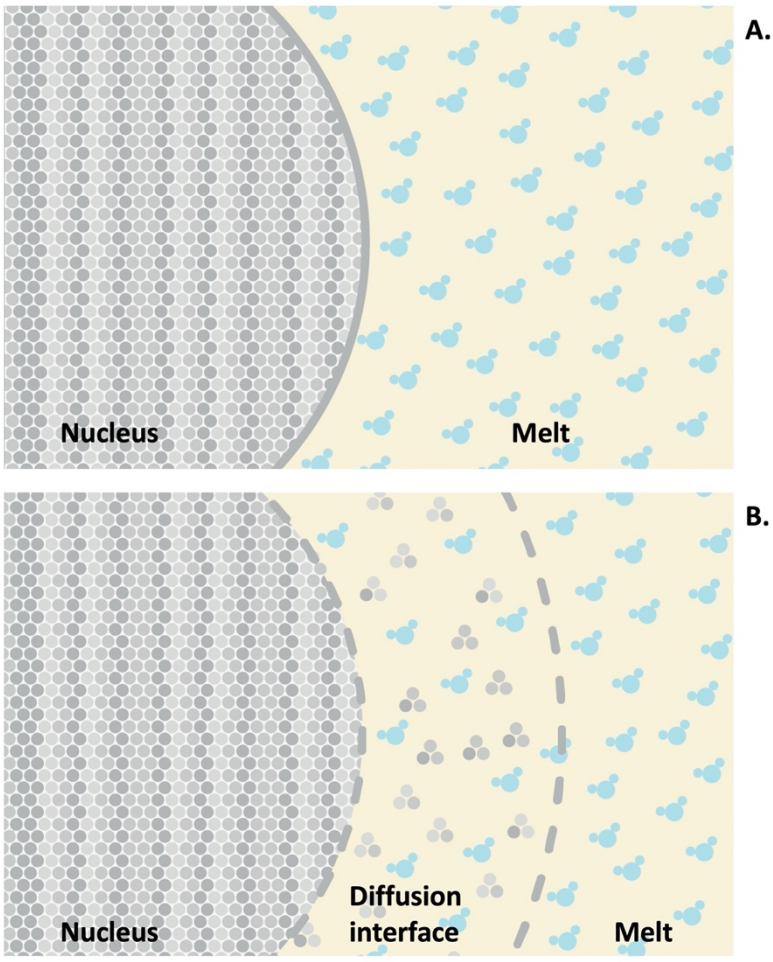

Figure 4. Schematic representation of the level of ordering at the melt-nucleus interface; grey filled circles – atoms (or molecules) of the growing nucleus in the melt; blue filled circles – water molecules in the melt; yellow – melt. **A.** Sharp melt-nucleus interface as described by the classical nucleation theory; **B.** Progressive melt-nucleus interface as describe by the diffuse interface theory

The interface between the crystal nucleus and the silicate melt is expected to be significantly poorer in water than the bulk melt (Rusiecka et al. 2020). The interfacial free energy will vary spatially with the diffuse interface (Hammer 2004). This will therefore influence the activation energy for the transport of elements across the melt-nucleus interface and the interfacial free energy, which also varies with the water content (Baker 1992; Hammer 2004). The interfacial free energy was therefore calculated using Hammer's (2004) empirical equation:

$$\sigma = -0.0176 * (H_2O) + 0.1121 \quad (7)$$

where H_2O is the interfacial water content. This equation, which was derived from experimentally determined values, is valid from 0 to 3 wt% interfacial water. The exact values used in this study will be discussed in further sections.

3. RESULTS

3.1. Summary of melting run products

Melting experiments were performed at 1070, 1040, 1000, 950 and 850 °C at 630 MPa, for durations of 96, 110 and 115 hours. Experimental conditions, total H_2O, phases present, and percent crystallization are summarized in Table 3 and images depicting the mineral phases and textures produced in the melting experiments are presented in Figure 5. The aim of the 1070 °C and 1040 °C experiments was to determine the bulk liquidus of our melt composition. Grain mounts were produced for these temperatures and mineral identification was not performed as we were only interested if crystals were present or not. The aim of the 1000, 950 and 850 °C experiments was to determine the saturation temperatures of quartz and feldspar in this melt composition, therefore, we focus here on the mineral assemblages and textures rather than composition evolution.

Table 3. Melting experiments run table.

	Final T (°C)	Time (h)	Total H_2O content (wt%)	Phases	% crystals (all phases considered)
MB43	1070	96	4.25	*gl*	0
MB45	1040	96	4.25	*gl, crystals (sil, crn)*	0
MB72	1000	110	4.22	*gl,sil,crn*	20
MB103	950	115	4.20	*gl,pl*	40
MB74	850	115	3.64	*gl,sil,crn,qtz,pl*	80

Table 3. Experimental run table showing the experimental conditions and the phases produced at 630 MPa for the melting experiments of MM45B. Total water content represents the amount of water added to the rock powder and the water content initially present in MM45B. *mgt* magnetite, *sil* sillimanite, *crn* corundum, *gl* glass, *qtz* quartz, *pl* plagioclase, *crystals* discussed in text.

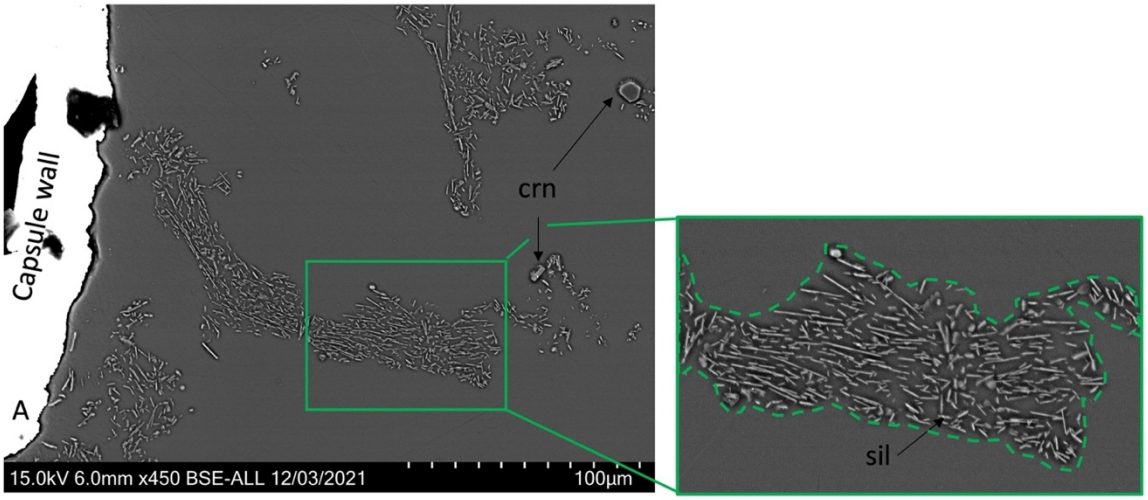

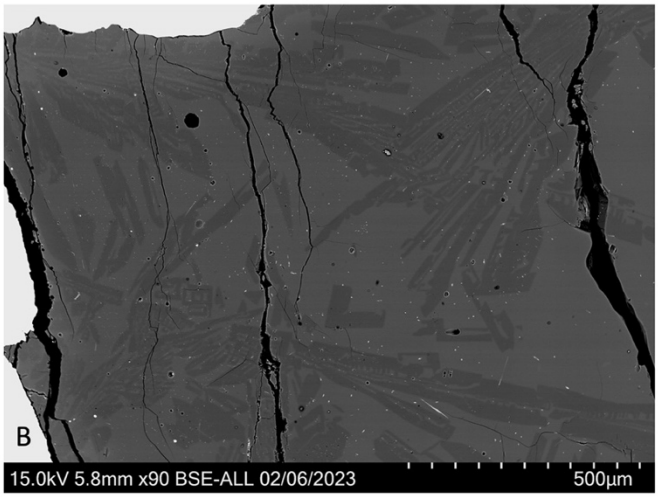

Figure 5. Backscattered electron images of the melting experimental run products, with the contrast and brightness adjusted in ImageJ; **A.** 1000°C, 630 MPa, 110 hours; Sillimanite and corundum crystals nucleating homogeneously; close up of sillimanite occurring in a cluster and following the outline of a remnant larger- scaled crystal; **B.** 950°C, 630 MPa, 115 hours; Large highly skeletal feldspar crystals occurring both homogeneously and heterogeneously on the capsule wall.

At 1070 °C, after 96 hours, no crystal was present while at 1040 °C, after 96 hours, crystals were present. Based upon lower temperature experiments (and crystallization experiments discussed in the next section), we can assume that sillimanite and corundum were the crystalline phases present at 1040 °C.

At 1000 °C, after 110 hours, sillimanite and corundum crystals were present. They display, respectively, prismatic lath-like and anhedral rounded and elongated habits of similar length. Both sillimanite and corundum occurred homogeneously in the melt, but large clusters mainly composed

of sillimanite seem to follow the outline of larger (at least one order of magnitude) remnant crystals (Fig. 5A).

At 950 °C, after 115 hours, large, typically greater than 150 μm on the short-axis, sodium-rich skeletal, almost feathery feldspar crystals were present as the only crystalline phase at these experimental conditions (Fig. 4B). Feldspar crystals are present both in the centre of the capsule and near its walls. The texture displayed by the feldspar crystals is indicative of rapid growth.

At 850 °C, after 115 hours, feldspar, quartz and sillimanite are present as a large crystalline framework. Feldspar occurs as sodium-rich tabular crystals, quartz occurs as hexagonal euhedral crystals and sillimanite as elongated, acicular crystals. It is difficult to determine if sillimanite nucleated or heterogeneously due to the high level of crystallinity (~80% crystallized). The sample appears to display a porphyritic texture.

Based upon these observations, the bulk liquidus of the Mt. Mica composition was defined as 1055 ± 15 °C due to the presence of crystalline phases at 1040 °C and the absence of crystalline phases at 1070 °C. The melting temperature of sillimanite and corundum was also set at this temperature as they are the first phases forming in our crystallization experiments. Based solely on the melting experiments, the saturation temperature of plagioclase would be 975 ± 25 °C since feldspar crystals were observed at 950 °C but not at 1000 °C, and the melting temperature of quartz was set at 900 ± 50 °C based on quartz crystals being observed at 850 °C, but not at 950 °C. However, the experimentally determined feldspar saturation temperature was not used because the feldspar crystals found in the run products of our melting experiments displayed rapid-growth features with textures unlike those seen in other melting experiments. The experiment was associated with large variations in amps supplied to the piston cylinder, which could indicate that the temperature was not constant throughout the experiment duration. We surmise that the

feldspars seen in the 950 °C melting experiment were newly grown after all the feldspar crystals initially present in the rock powder were melted due to the variations in temperature. Data from the 950°C experiment were therefore not considered and, instead of the experimental results, theoretical data from rhyolite-MELTS were used for the melting temperatures. For feldspar and quartz, the saturation temperatures were respectively set to 885 °C and 875 °C, which are the equilibrium liquidus temperatures for plagioclase and quartz for the Mt. Mica composition (calculated by rhyolite-MELTS).

3.1. Summary of crystallization run products

Crystallization experiments were performed at 1000, 900, 850, 800, and 750 °C at 630 MPa for durations ranging between 0.3 and 211 hours. Experimental conditions, total H_2O in the capsules, phases present, and percent crystallization are summarized in Table 4. Sillimanite, corundum, glass, iron oxides, quartz, and feldspar were present in the experimental run products. Images depicting the mineral phases and textures produced in the crystallization experiments are presented in Figures 6 to 9.

All experiments are dominated by glass (quenched melt), with the highest degree of crystallinity (35%) achieved at the lowest temperature, 750 °C. The quenched melt composition varies with the degree of undercooling and duration of experiments, which will be further explored in the next section. However, the melt composition is homogeneous within each run product, even in the vicinity of crystals. For all the run conditions, the duplicate capsules displayed the same mineral assemblage and textures, except for the 750 °C, 2-hour experiment, where the two capsules contained different mineral assemblages, and at 900°C for 29 hours, where one capsule failed. The

other capsules, however, only slightly varied in total percent crystallization and modal abundance of each phase (both varied by ~ 1-2 relative percent).

At 1000 °C, no crystals were detected after 6 hours. After 44 hours, iron oxide, an aluminosilicate mineral, and corundum crystals nucleated. The aluminosilicate is thought to be sillimanite due to the pressures and temperatures at which the experiments were performed (Holdaway 1971). Corundum crystals were anhedral or elongated, whereas sillimanite crystals were euhedral, displaying rhombic habits (Fig. 6A). Both minerals preferentially nucleated near, or directly on, the capsule walls; the centre of the capsule was almost free of any crystals. Iron oxide crystals were subhedral and nucleated both homogeneously and heterogeneously, with larger crystals (5 μm) mainly nucleating with corundum and sillimanite, while smaller crystals (0.5 μm) nucleated homogeneously in other regions of the capsule.

Table 4. Crystallization experiments run table.

	Final T (°C)	ΔT (°C)	Time (h)	Total H_2O content (wt%)	Phases	Total percent crystallization
MB52	1000	-55	6	4.19	*gl*	0
MB53	1000	-55	6	4.11	*gl*	0
MB58	1000	-55	44	4.27	*gl+sil+crn+ox*	2
MB60	1000	-55	44	4.18	*gl+sil+crn+ox*	2
MB67	900	-155	0.5	4.26	*gl+sil+crn*	2
MB68	900	-155	0.5	4.14	*gl+sil+crn*	2
MB61	900	-155	5	4.18	*gl+sil*	4
MB62	900	-155	5	4.21	*gl+sil*	4
MB64	900	-155	29	4.28	*gl+sil+crn*	2
MB69	900	-155	211	4.23	*gl+sil+crn*	<1
MB70	900	-155	211	4.28	*gl+sil+crn*	<1
MB80	850	-205	115	4.23	*gl+sil+crn+qtz+ox*	3
MB81	850	-205	115	4.31	*gl+sil+crn+qtz+ox*	2 ~ 1
MB105	850	-205	5	4.23	*gl+sil+crn+ox*	3
MB106	850	-205	5	4.27	*gl+sil+crn+ox*	2
MB87	800	-255	115	4.26	*gl+sil+crn+qtz+pl+ox*	25
MB88	800	-255	115	4.19	*gl+sil+crn+qtz+pl+ox*	25
MB110	800	-255	120	4.27	*gl+sil+crn+qtz+pl+ox*	35
MB111	800	-255	120	4.23	*gl+sil+crn+qtz+pl+ox*	35
MB114	800	-255	0.3	4.23	*gl+crn+ox*	2
MB115	800	-255	0.3	4.27	*gl+crn+ox*	2
MB118	800	-255	4	4.23	*gl+sil+crn+ox*	4
MB119	800	-255	4	4.23	*gl+sil+crn+ox*	6
MB89	750	-305	5	4.25	*gl + sil*	2
MB90	750	-305	5	4.25	*gl+sil*	2
MB91	750	-305	28	4.27	*gl+qtz+sil+crn+unknown phase+ox*	15
MB92	750	-305	28	4.28	*gl+qtz+sil+crn+unknown phase+ox*	15
MB94	750	-305	2	4.23	*gl+sil+crn*	5
MB95	750	-305	2	4.28	*gl+sil*	5

Table 4. Experimental run table showing the experimental conditions and the phases produced at 630 MPa following homogenization of the melt at 1100 °C for 24 hours for the crystallization experiments of MM45B. *ox* oxide, *sil* sillimanite, *crn* corundum, *gl* glass, *qtz* quartz, *pl* plagioclase, *unknown phase* discussed in text.

At 900 °C, after 0.5 hours, both sillimanite and corundum crystals were present in the experiment, displaying the same habit as crystals present at 1000 °C. In the 5-hour experiment, only sillimanite crystals were found. They had rhombic habits which varied greatly in size (between 0.3 and 61 μm) (Fig. 6B). Sillimanite nucleated homogeneously everywhere in the capsules, but the degree of crystallinity varied randomly along the length of the capsule. Radial, crystalline aggregates were found in regions with higher crystallinity (Fig. 6C), whereas in other regions sillimanite crystals were randomly arranged (Fig. 6B,C). In the 29-hour experiment at 900 °C, sillimanite and corundum nucleated. Most crystals nucleated near the capsule walls while the centre of the capsule was nearly free of crystals. Sillimanite crystals varied in size (between 1 and 54 μm), had rhombic habits, and some crystals were hollow. All corundum crystals are euhedral and have an acicular habit (habit displayed in Fig. 8C), unlike the corundum crystals produced at a lower degree of undercooling. The majority of crystals appear to have grown parallel to the walls of the capsules, most notably the corundum crystals. The 211 hour-long experiment displayed the same mineralogy and textures as in the 29-hour experiment.

At 850 °C, after 5 hours, sillimanite and corundum both nucleated homogeneously. Sillimanites have rhombic habits (Fig. 7A). The corundums are most commonly anhedral, but some crystals show elongated or rounded habits, the elongated crystals varying in size between 2 and 33 μm and the rounded crystals between 9 and 26 μm (Fig. 7A). The corundums are also systematically surrounded by crystalline halos that are qualitatively richer in sodium and silicon, and poorer in aluminum and oxygen than the corundums at the centres of the halos (Fig. 7A,B). Oxides nucleated at the edge of the corundum and are also, when present, enclosed in the crystalline halos. In the 115-hour experiment, rhombic sillimanite crystals, which are sometimes hollow, nucleated. They are an order of magnitude larger than sillimanite that crystallized at higher

temperatures. Long acicular corundum crystals (between 23 and 103 μm) are also present and appear to mainly have nucleated parallel to the capsule walls (Fig. 7C). Corundum crystals mainly nucleated in the vicinity of the capsule walls (Fig. 7C), while sillimanite nucleated homogeneously everywhere in the capsule. Quartz nucleated heterogeneously on the capsule wall as euhedral crystals (Fig. 7C). In other instances, quartz crystals have rounded irregular habits and completely enclose small needle-like, crystals, giving a texture similar to fibrolite. Due to the small size of the needles, it was not possible to obtain EDS analyses without analyzing the glass or the surrounding quartz, but, based on qualitative analysis of elemental EDS maps, these needles appear to only be composed of Al_2O_3 and are most-probably corundum crystals. Iron oxides were present in all the experiments performed at 850 °C. No feldspar was found in any experiments at 850 °C.

At 800 °C, after 0.3 hours, anhedral crystals of corundum and oxides are present. Corundum crystals nucleated homogeneously in the capsule and oxides nucleated both heterogeneously with the corundum crystals and homogeneously in the centre of the capsule. The corundums are also surrounded by crystalline halos with similar compositions to those analyzed in higher-temperature experiments (Fig. 7A,B). In the 4-hour experiment sillimanite, corundum and oxide crystals nucleated homogeneously. Sillimanites occurred mainly as acicular or hollowed rhombic crystals while corundums have anhedral elongated habits and are surrounded by crystalline halos. In some cases multiple corundum crystals are clustered inside crystalline halos encapsulating all of them. The 115-hour experiment contained sillimanite and corundum crystals that nucleated homogeneously. Corundum crystals are mainly elongated or rounded and oxides systematically nucleated at the edges of the crystals. Similar to the 4-hour experiment, clusters of corundum also occurred inside crystalline halos. Sillimanite crystals are present as rhombic and acicular crystals. Rounded and irregular quartz nucleated heterogeneously with sillimanite and

corundum crystals, and on the capsule walls (Fig. 8C). Large skeletal feldspar spherulites also formed heterogeneously on the capsule walls (Fig. 8A). Sillimanite and corundum crystallized before quartz and feldspar, as indicated by the latter enclosing the former (Fig. 8C). It is, however, not possible to determine the order of crystallization of quartz and feldspar because they are never in direct contact with one another. In the 120-hour experiment, the same phases are present as in the 115-hour experiment. However, acicular crystals of sillimanite are arranged in radial aggregates, corundum crystals are encircled by crystalline halos, and the feldspar spherulites are present in a higher modal abundance and form more regular rims. The feldspar spherulites mainly nucleate heterogeneously on the capsule wall, but a few smaller spherulites also nucleated homogeneously (Fig. 8B). Vesicles are present in the vicinity of isolated plagioclase crystals and spherulites (Fig. 8A,B). The vesicles do not perfectly follow the edges of crystals, some occur directly on the crystal whereas others extend further into the melt. The quantity of vesicles also seems to increase with the size and the quantity of spherulites present, with 2-3 vesicles around isolated crystals of 50 μm and approximately 30 around large 700 μm spherulites. These vesicles were only observed in the 120-hour experiments. These vesicles are similar to those described in previous work (e.g., Baker and Freda 2001, Sirbescu et al. 2017, Rusiecka et al. 2020).

At 750 °C, 2 hours, the two capsules are not consistent, one crystallizing only sillimanite and the other, sillimanite and corundum. This discrepancy between the two capsules only occurred at this duration and temperature. In both capsules, sillimanite is rhombic and nucleated homogeneously and randomly in the capsule. Corundum crystals also nucleated homogeneously, and the crystals are anhedral and elongated. In the 5-hour experiment at 750 °C, only sillimanite nucleated, and most crystals display a subhedral rhombic habit; a few bladed sillimanite crystals are also present. After 28 hours, sillimanite, corundum, quartz and iron oxides are present,

displaying the same morphology as at 800 °C for 120 hours (Fig. 9B,C). Moreover, the fibrous corundum seen in the 850 °C, 115-hour experiment, is also present, enclosed by irregular rounded quartz crystals (Fig. 9C). Iron oxides were present after 28 hours. No feldspar was found in any experiments at 750 °C.

Notably, the 750 °C and 28 hours experimental run products contain fan, bowtie and spherical spherulites (following Lofgren's (1974) terminology) that appear to be formed by small fibres of an unknown phase. The spherulites occur both homogeneously in the melt and heterogeneously on the capsule wall or around corundum and sillimanite crystals (figures 9A,B). The latter indicating that the spherulites formed after corundum and sillimanite. Possibly due to the small size of the fibres in the spherulites, the EDS quantitative analyses of the unknown phase were not conclusive. However, qualitative EDS elemental maps indicate that they are richer in silicon and poorer in sodium compared to the melt.

3.2 Corundum morphology, texture, and composition

Corundum was the most rapid phase to nucleate in this study, with the shortest nucleation delay in this study of 0.3 hours. It first nucleated at 55°C under the MM45B liquidus. It mostly displayed highly anhedral habits except in some instances where corundum crystallized as small needles (between 3 and 103 μm) and possibly fibrous crystals. These aluminum-rich fibrous crystals are similar to the abundant mullite needles in the experiments described by Holtz et al. (1992a). Further analyses would be necessary to confirm their composition. Corundum was also associated with crystalline halos, which started being observed at temperatures at or below 850 °C. The corundum displays no significant change in composition over our range of experimental

conditions, the mean of the composition of the each run product being within 1 sigma of the global mean.

3.3 Sillimanite morphology, texture, and composition

Sillimanite is the phase with the highest nucleation density and a large variability in crystal habits, displaying rhombic, hollowed and acicular shapes of varying sizes. The crystals also displayed a euhedral habit in all experiments. Sillimanite first nucleated 55 °C under the MM45B liquidus and quickly, with its shortest nucleation delay being only 0.5 hours. Sillimanite appears to only crystallize homogeneously in the capsule, except when displaying radial crystal aggregates. The radial arrangement did not however occur systematically with increasing undercooling and time. Similar to corundum, the composition of sillimanite does not significantly change over our range of experimental conditions.

3.4 Quartz morphology, texture, and composition

Quartz first nucleated at ΔT -205 and took at least 28 hours to form. Quartz displayed the least variability in crystal habits compared to other minerals in this study. It nucleated principally on the capsule wall or on corundum crystals as rounded irregular quartz and also as prismatic euhedral hexagonal crystals. In our experiments there was no observed relationship between the crystal habit, the degree of undercooling, and duration. The modal abundance of quartz, however, increased as the degree of undercooling and experimental duration increased. The quartz composition remained within one sigma value for each experiment. No evidence for stuffed quartz was observed, though complementary analyses would be required to confirm. Quartz did not display significant variation in composition over our range of experimental conditions.

3.5 Feldspar morphology, texture, and composition

Feldspar had the longest nucleation delays, at a ΔT of -255 °C (at 800 °C), and the lowest nucleation density compared to all the phases crystallized in this study. The feldspar first started nucleating after 155 hours. The crystals, in the form of spherulites, were the largest, reaching sizes up to 600 μm in width. Most spherulites nucleated heterogeneously on the capsule wall, but there are also instances where smaller spherulites nucleated homogeneously. These isolated spherulites were one order of magnitude smaller than the spherulites that nucleated on the capsule wall. All the spherulites were highly skeletal and contained melt inclusions. Feldspar only nucleated in one experiments and therefore, given the small size of our dataset, it was not possible to clearly determine any relationships between the degree of undercooling and the crystal habit. Based on EDS analyses, these spherulites are richer in sodium than the melt, but also contain varying, but low, concentrations of calcium and potassium. The composition of the most sodium rich crystals was $Ab_{89}An_7Or_4$ while the least sodium rich crystals had a composition of $Ab_{87}An_8Or_4$, indicating that these are plagioclase crystals. No intra-spherulite compositional variations were observed, but different spherulites had varying sodium, potassium and calcium content.

3.6 Melt composition

The composition of the quenched glass, representative of the melt present in the experiments, remains relatively constant, similar to the bulk composition, with an increasing degree of undercooling in Al_2O_3 and S_iO_2, which can be explained by the low variations and low value in percent crystallization. There is a small decrease in Na_2O and increase in CaO and K_2O, which coincides with the appearance of sodium-rich feldspar spherulites (Fig. 10).

3.7 Raman spectroscopy analyses

The Raman spectroscopy analyses were inconclusive but demonstrated that the tested run products still contained water. However, we did not obtain quantitative water concentrations from the quenched glass in these experiments.

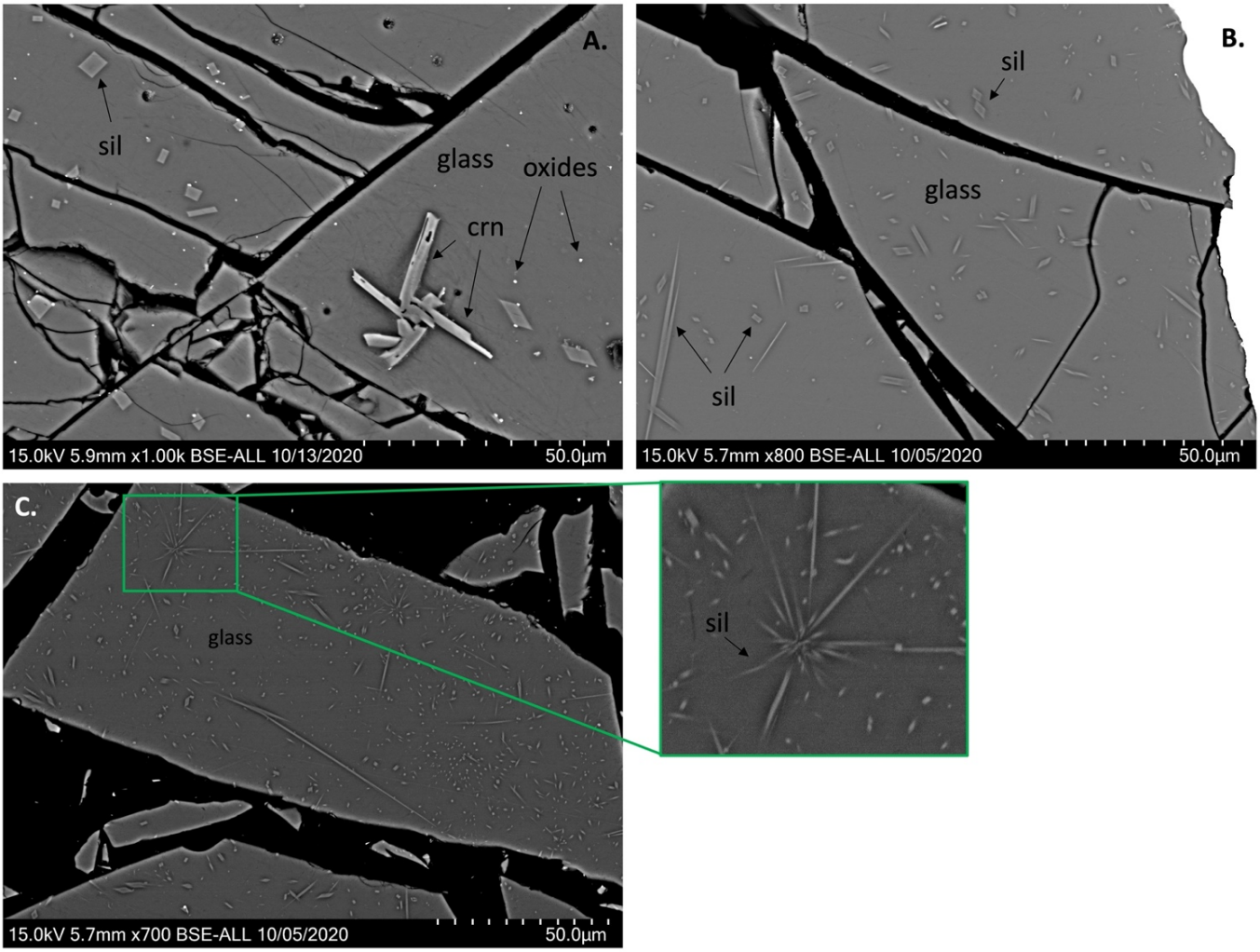

Figure 6. Backscattered electron images of the crystallization experimental run products, with enhanced contrast and brightness; **A.** 1000 °C, 630 MPa, 44 hours; sillimanite and corundum crystals displaying respectively rhombic and anhedral habits. Small oxides nucleated both homogeneously and heterogeneously with sillimanite and corundum crystals. Most of the capsule is occupied by remaining melt, which becomes glass after being quenched; **B.** 900°C, 630 MPa, 5 hours; sillimanite crystals randomly nucleating homogeneously in the entire capsule; **C.** 900°C, 630 MPa, 5 hours; sillimanite crystals randomly nucleating homogeneously in the entire capsule; close-up of a radial aggregates of sillimanite crystals; close-up of a radial aggregates of sillimanite crystals.

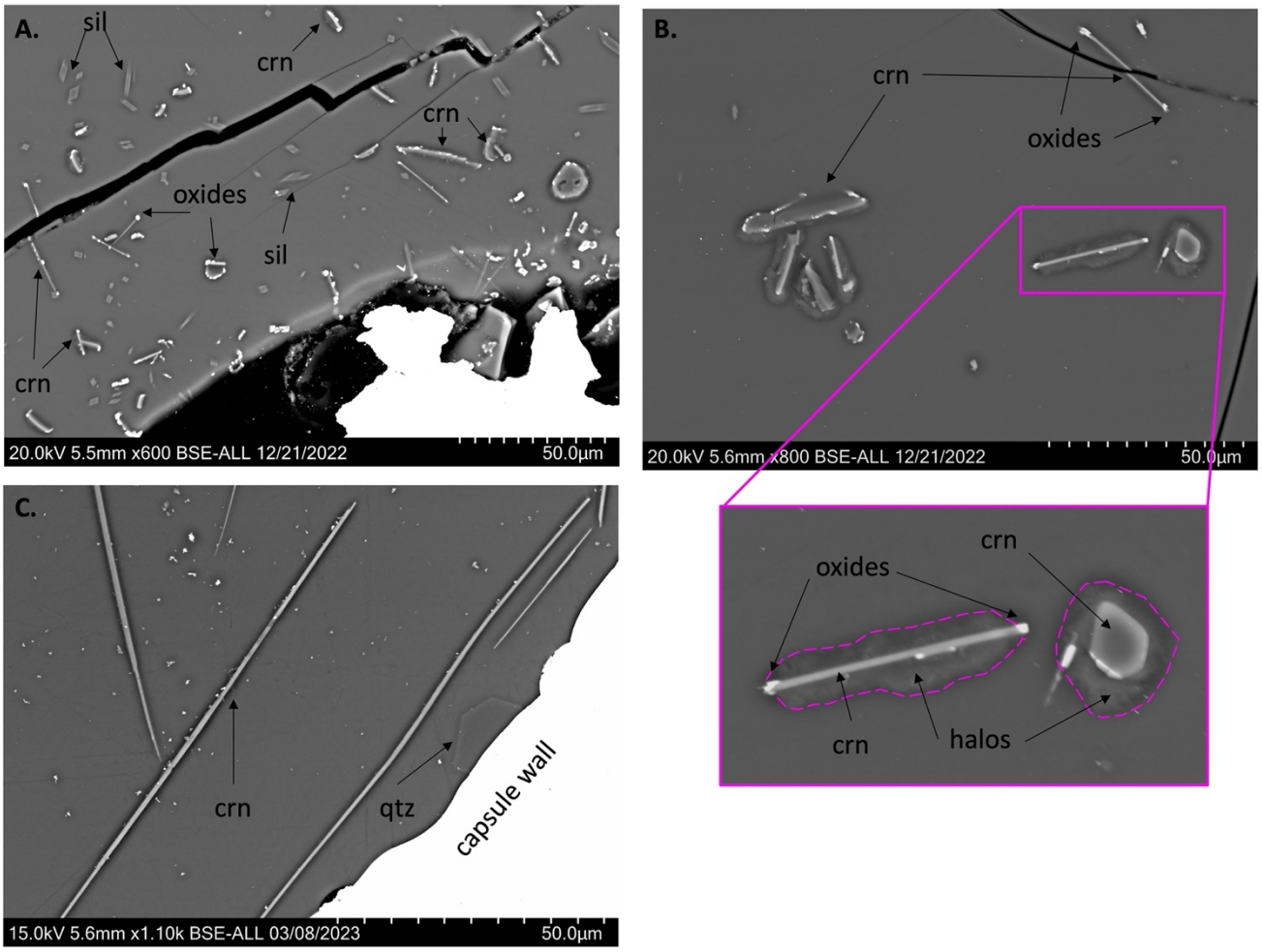

Figure 7. Backscattered electron images of the crystallization experimental run products, with enhanced contrast and brightness; **A.** 850°C, 630 MPa, 5 hours; sillimanite crystals displaying rhombic habits and corundum crystals displaying anhedral, elongated or rounded habits. Iron oxides nucleated heterogeneously at the edge of the corundum crystals; **B.** 850°C, 630 MPa, 5 hours; close-up of the crystalline halos surroundings corundum crystals and iron oxides **C.** 850°C, 630 MPa, 115 hours, long acicular corundum crystals nucleating parallel to the capsule wall and euhedral quartz crystals nucleating on the capsule wall

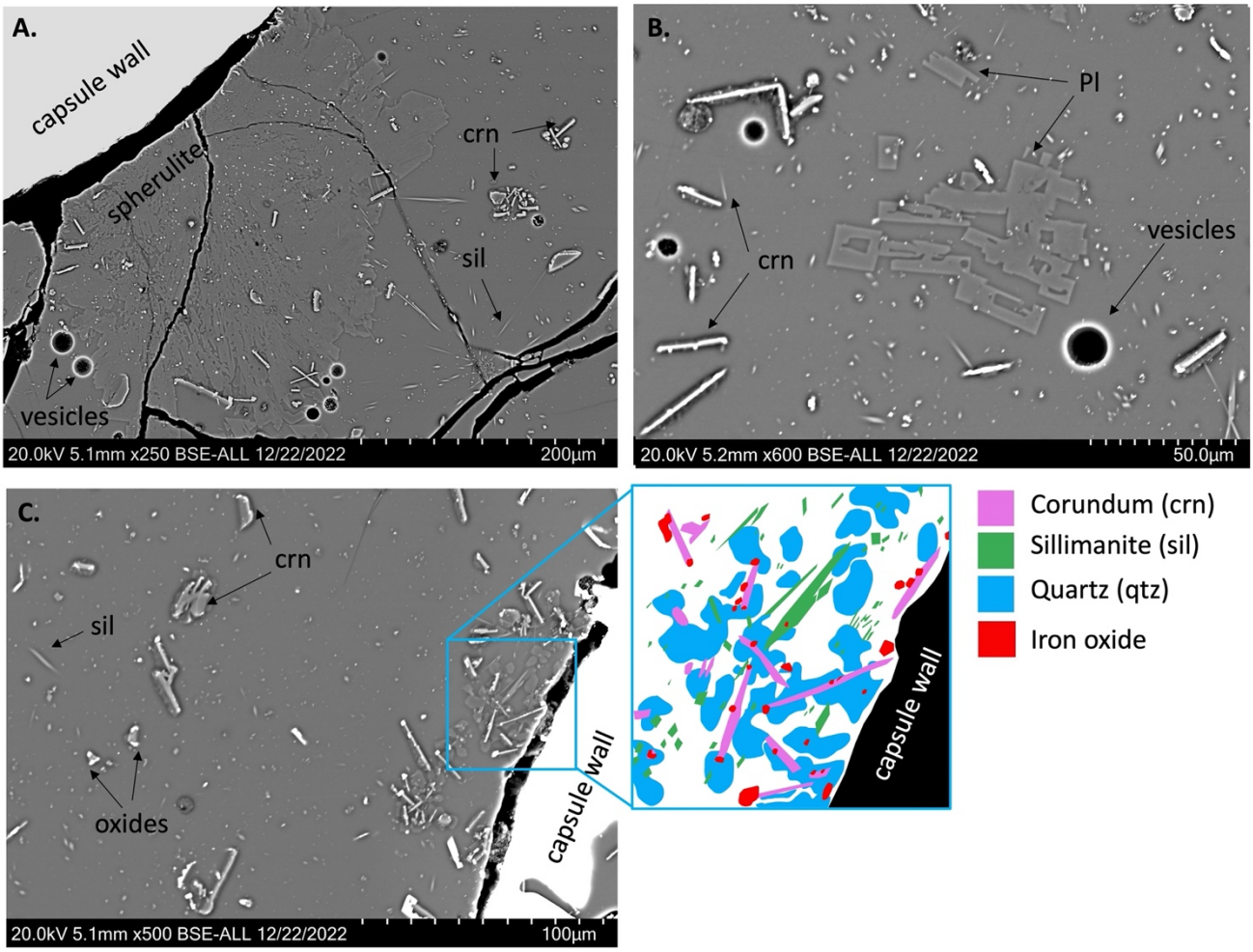

Figure 8. Backscattered electron images of the crystallization experimental run products, with the contrast and brightness increased in ImageJ; **A.** 800 °C, 630 MPa, 120 hours; Skeletal spherulite of plagioclase surrounded by epoxy-filled vesicles. Sillimanite crystals occurring as radial aggregates; **B.** 800 °C, 630 MPa, 120 hours; isolated skeletal crystal of plagioclase surrounded by epoxy-filled vesicles. Elongated anhedral corundum crystals are surrounded by crystalline halos previously described; **C.** 800 °C, 630 MPa, 120 hours; close-up showing the order of crystallization of the crystalline phases, with rounded irregular quartz enclosing corundum, sillimanite and iron oxides

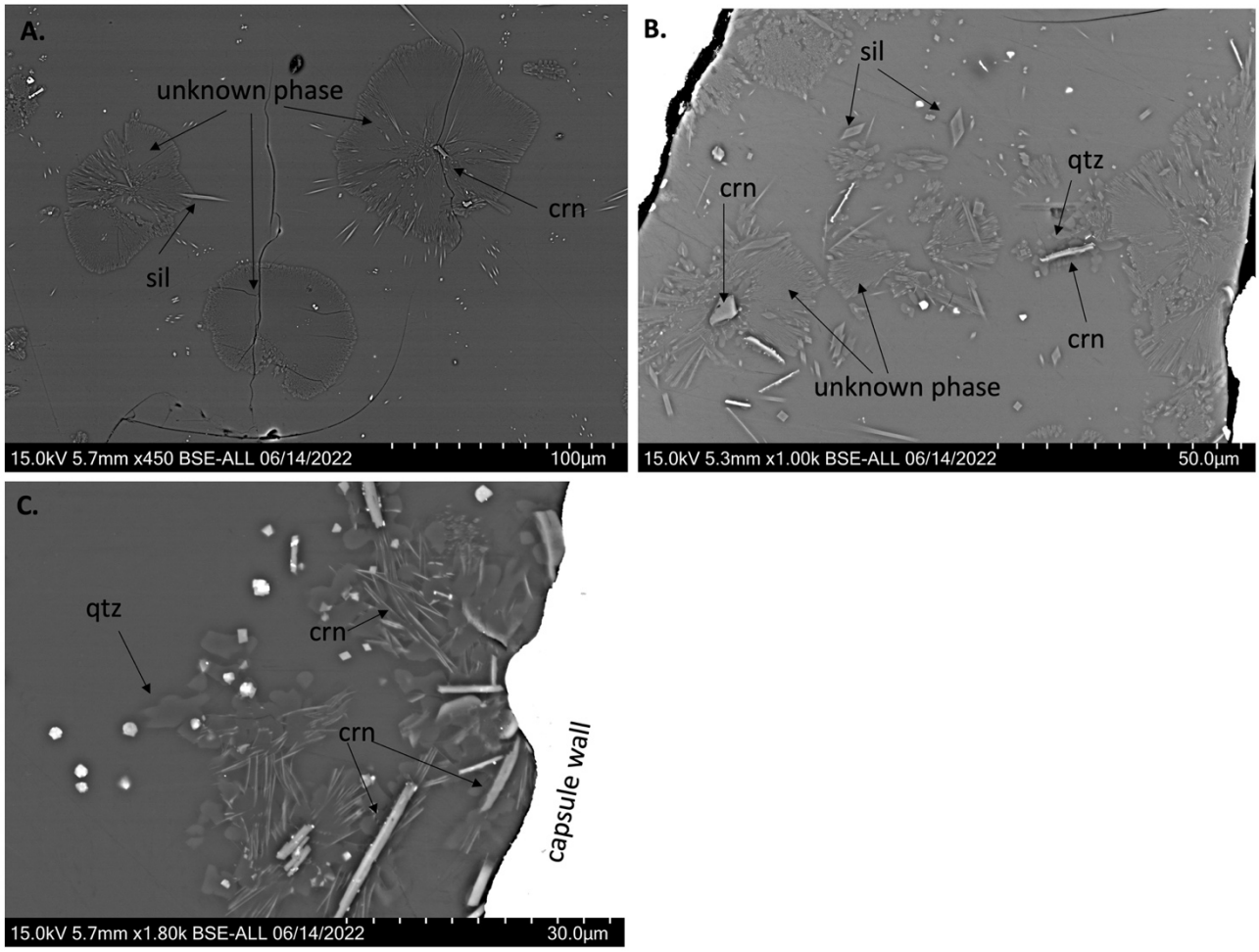

Figure 9. Backscattered electron images of the crystallization experimental run products, with the contrast and brightness enhanced; 750 °C, 630 MPa, 28 hours; **A.** Spherulites nucleating homogeneously in the melt, enclosing sillimanite and corundum crystals; **B.** Fan, bowtie and spheric spherulites nucleating both homogenously and heterogeneously around corundum crystals and on the capsule wall**; C.** Rounded irregular quartz crystals nucleating around elongated and fibrous corundum crystals. Iron oxides nucleate both homogeneously and heterogeneously.

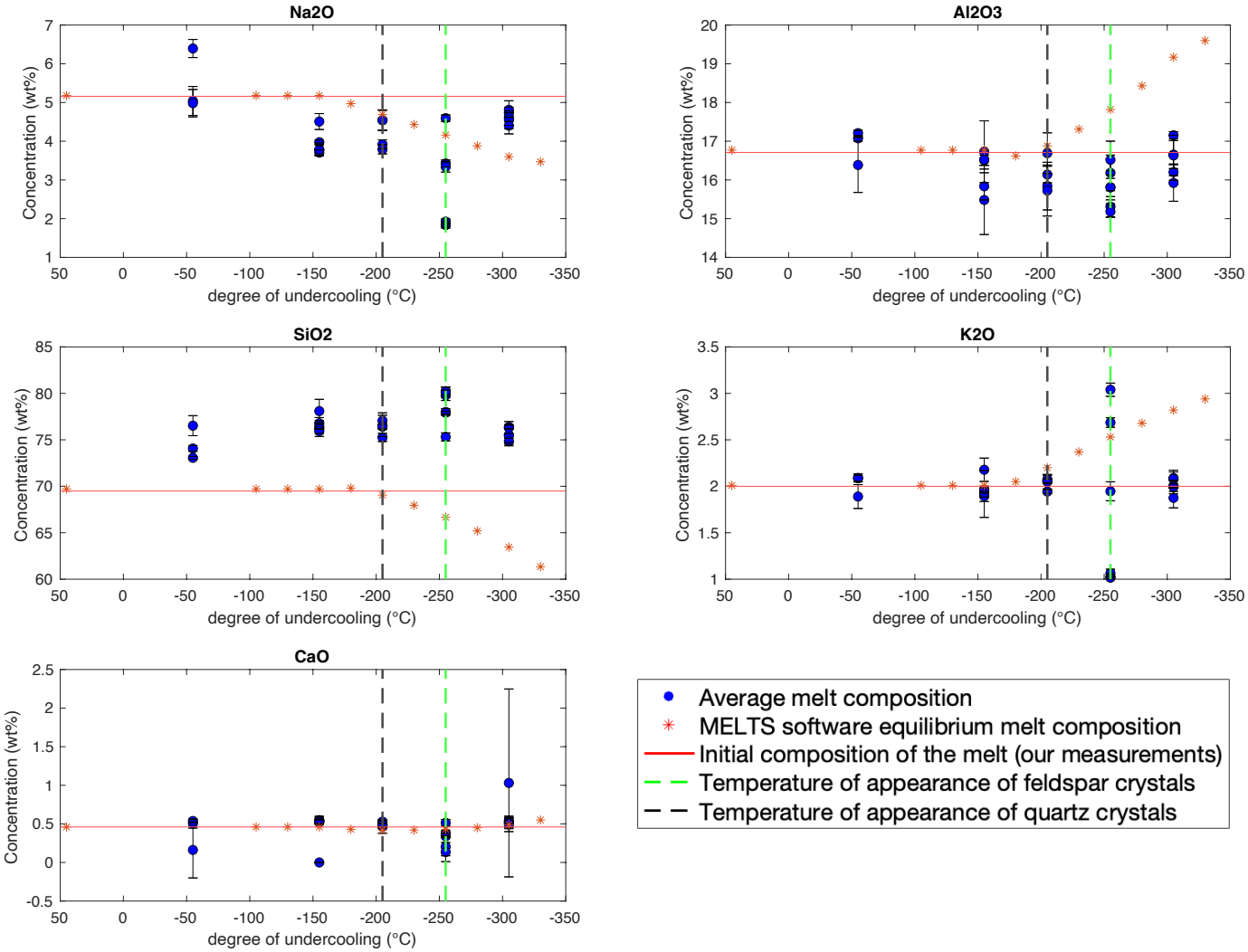

Figure 10. Melt composition evolution (wt%) during crystallization experiments, with respect to the degree of undercooling (°C). The average composition of the melt at each run conditions was measured by EDS quantitative analyses of the quenched glass. The standard deviation was calculated from the available dataset (minimum of five points) at each run condition and is shown as error bars for each datapoint. Blue points – Average oxide concentration; Red stars – MELTS equilibrium oxide concentration; red line – Initial oxide concentration; Back dotted line – Temperature of appearance of quartz crystals; Green dotted line – Temperature of appearance of feldspar crystals

4. DISCUSSION

4.1 Parameters used in Equation 3 and selection criteria

We calculated nucleation delay times for the Mt. Mica pegmatite with 4.25 wt% water and compared the model to our experimental results. The nucleation delay curves of sillimanite, corundum, quartz and feldspar showed varying degrees of agreement with our experimental results (Fig. 11), with quartz showing good levels of agreement, sillimanite and corundum showing good levels of agreement at high degrees of undercooling and feldspar showing good levels of agreement though additional data are required to constrain the nucleation curve of feldspar at lower degrees of undercooling. These nucleation curves were adjusted to the closest degrees of agreement with the experiments by varying the interfacial water content in Equation 3, as fully described in section 2.3.

In Equation 3, the size of the structural unit (a) and the Gibbs free energy per unit volume are fixed parameters, meaning that for one mineral, these values are not varied. Both the activation energy (E_a) and the interface free energy (σ) can be written in terms of the water content of the melt-nucleus interface (cf. Rusiecka et al., 2020) and therefore, only one parameter can be adjusted in Equation 3 to determine the fit between the theoretical model and our experimental data. It is not possible to measure the interfacial water content, hence this is why we adjusted this parameter. The interfacial water content (Equation 7) therefore becomes a "free-parameter", between values of 0 and 3 wt% water, that can be varied to adjust the calculated nucleation delay curves to our experimental results in order to reach the highest level of agreement between theory and experiments.

The equilibrium saturation temperatures calculated by MELTS also can be adjusted to match the experimentally determined values from crystallization experiments because the liquidus

determined by MELTS is not the same as the experimental one. This adjustment does not impact the accuracy of our results as they are reported and analyzed with respect to the ΔT values and not the absolute temperatures (cf. Rusiecka et al. 2020).

For sillimanite and corundum, since the vast majority of crystals nucleated homogeneously, the heterogeneous nucleation correction was not considered. However, all of quartz and most plagioclase crystals nucleated heterogeneously on the capsule wall or on previously nucleated phases, and therefore, Equation 4, describing heterogeneous nucleation, was applied. This equation requires the value of the inner contact angle (Equation 5). The values determined by Rusiecka et al. (2020) were used due to the low modal abundance feldspar and quartz in our experimental run products. They measured the contact angles between 79 of their feldspar spherulites and the capsule wall in various experiments. The mean of their measurements, and the value we used, is 89 ° (the standard deviation of Rusiecka et al.'s measurements was $\pm$ 22 °). However, varying the inner contact angle influences the nucleation delay by less than one order of magnitude for both quartz and feldspar, demonstrating that it is not the variable with the highest impact of the nucleation delay.

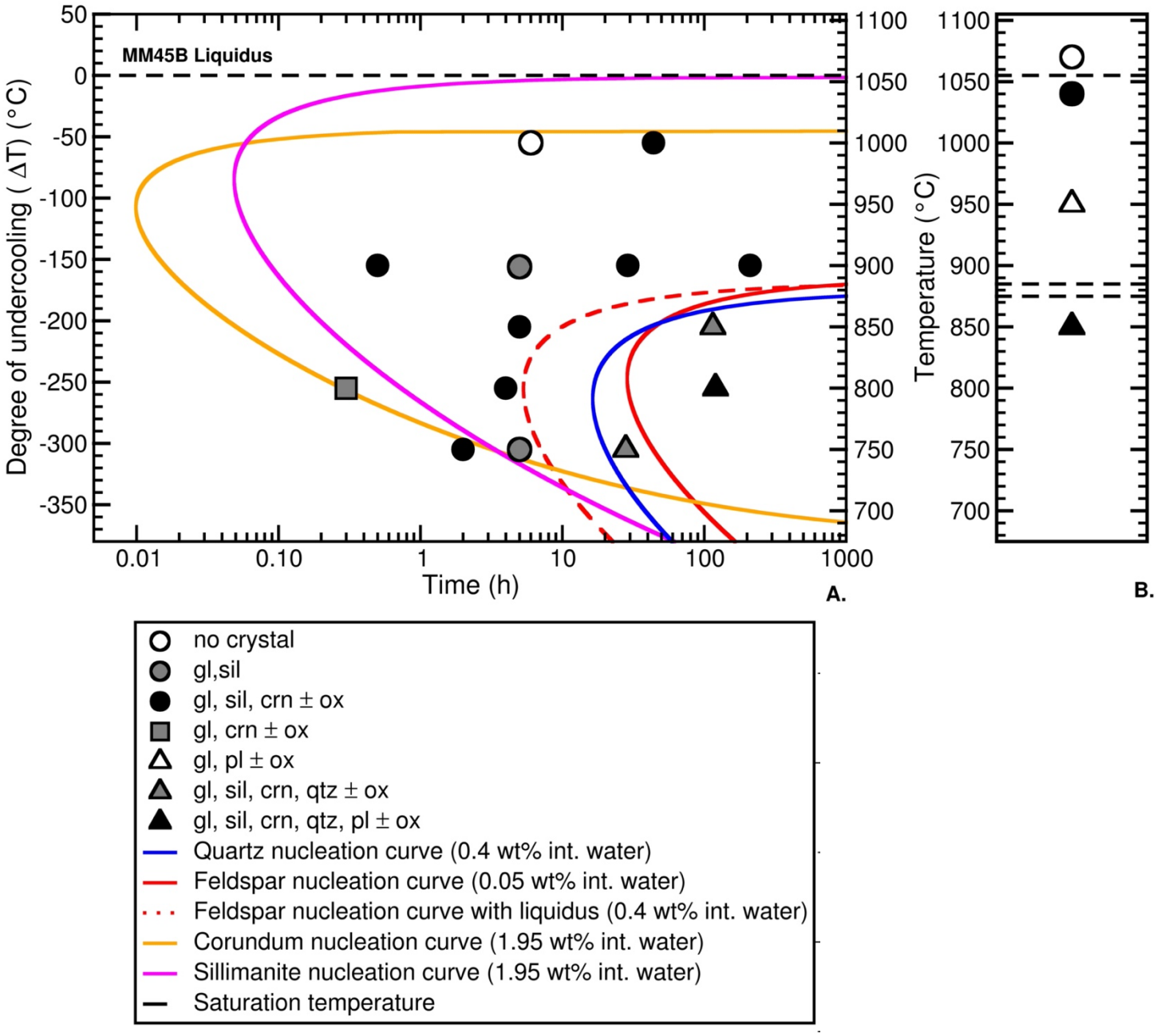

Figure 11. A. Nucleation delay of sillimanite, corundum, quartz and feldspar in hydrous peraluminous granitic melt. The curves calculated for homogeneous nucleation for sillimanite and corundum and the curves for quartz and feldspar were calculated for heterogeneous nucleation with a wetting angle of 89 °; the water concentration used for the calculation of the activation energy and the interfacial energy is 1.95 wt. % for sillimanite and corundum, 0.4 wt% for quartz and 0.05 wt% for feldspar. Symbols represent crystallization experimental run products; **B.** Results of melting experiments and saturation temperatures for sillimanite, corundum, quartz and feldspar was set to 1055 °C, 1010 °C, 885 °C and 875 °C. Symbols represent melting experimental run products.

4.2 Level of agreement between experiments and modelled nucleation delay curves

When compared to our experimental data, Equation 3 accurately described the nucleation delay of corundum and sillimanite in typical granitic melts at temperatures below 900 °C (high degrees of undercooling); the agreement is within a factor of 2 (Fig. 11). However, at higher temperatures (low degrees of undercooling), there is a significant difference between the nucleation curves of sillimanite and corundum and our experimental data, with one crystal-free experiment plotting within our nucleation curves and one corundum-free experiment plotting at a delay where corundum should have nucleated (Fig. 11). At these high temperatures, the level of agreement between experimental and theoretical nucleation delays for corundum and sillimanite is within a factor of 100. For both aluminum-rich minerals, the highest level of agreement was obtained with an interfacial water content set to 1.95 wt%, adjusted to a liquidus value of 1055°C for sillimanite and 1010 °C for corundum, giving an activation energy value of 165.1 kJ/mol and an interfacial free energy value of 0.07778 J/m^2. The adjusted values fall within the range of interfacial water content values for which the activation energy and the interfacial free energy equations are valid (i.e., between 0 and 3 wt%). This value is, however, much higher than the interfacial water value used by Rusiecka et al. (2020) for quartz and feldspar nucleation delay in the melt they studied, 0.5 $\pm$ 0.1 wt%.

Equation 3 with the heterogeneous correction described by Equations 4 and 5, accurately described the nucleation delay of quartz (Fig. 11). The highest level of agreement was found with an interfacial water content set to 0.4 wt%, giving an activation energy value of 221.9 kJ/mol, and an interfacial free energy value of 0.105 J/m^2. This adjusted water content is also within the range of interfacial water content values for which the activation energy and the interfacial free energy

equations are valid (i.e., between 0 and 3 wt%). This interfacial water is also in agreement with Rusiecka et al. (2020) value used for quartz.

There is good agreement between the feldspar experimental and modelled nucleation delay data. The highest level of agreement, within a factor of 5, was reached with an interfacial water content of 0.05 wt%, where one feldspar-free experiment plots within our feldspar nucleation delay curve (Fig. 11). An interfacial water content set to 0.05 wt% yields an activation energy value of 234.7 kJ/mol and an interfacial free energy value of 0.1112 J/m^2. Notably, the interfacial water content that yields the nucleation curve with the highest degree of agreement with the feldspar experimental data was much lower than the interfacial water content of 0.4 wt% set for quartz in our study. The feldspar interfacial water content was also much lower than Rusiecka et al. (2020), who applied the same interfacial water content of 0.5 $\pm$ 0.1 wt% for both the feldspar and quartz nucleation curves. In our study, applying the same water content for feldspar than for quartz (0.4 wt% water) yielded poor level of agreement, within a factor of 24, between the theoretical and experimental data for feldspar and was therefore not chosen (Fig. 11).

The discrepancies between the theoretical model and experimental results could be potentially caused by the nature of our petrological observations. Since we are surveying a 2D surface to extrapolate observation of a 3D volume, it is possible we overlooked some crystallizing phases. Moreover, nucleation remains a stochastic process and nucleation theory is indeed a statistical prediction (Kalikmanov 2013; Neuville et al. 2020). It is therefore statistically possible that a run product fails to nucleate a phase even if it is favoured. This behaviour was plausibly exhibited by our 750 °C, 2-hour run where the two capsules nucleated different mineral assemblages. The stochastic nature of nucleation could also explain the difference in percent crystallization observed between capsules of experiments at the same run conditions.

Following the diffuse interface theory (DIT), the melt at the interface should be poorer in water than the bulk melt, which coincides with our results, as the adjusted interface water contents for corundum, sillimanite, quartz and feldspar are smaller than the bulk water content of our melt of 4.25 wt%. Corundum, sillimanite, plagioclase, and quartz, however, have different interfacial water concentrations. We speculate that these differences could hypothetically be explained by the differing abilities of these nominally anhydrous minerals to incorporate water into their structures. Sillimanite can contain to 200 ppm wt% water while quartz can incorporate up to 82 ppm wt% (Rossman 1996). Considering that the interface between the growing nucleus and the melt has intermediate properties between the crystal and melt (Gránásy 1993), if sillimanite can incorporate more water into its structure, the sillimanite-melt interface's water content could be higher than the quartz-melt interface, thus explaining the higher modelled water content at the interface between the alumina-rich minerals and the melt than at the quartz-melt interface.

We could not find similar data for corundum and plagioclase water incorporation. However, because of the high interfacial water content value set for corundum and the low interfacial water content set for plagioclase, we could hypothesize that corundum can incorporate more water in its structure than plagioclase, analogous to the behaviour exhibited by sillimanite and quartz.

We recognize that other studies (e.g., Devineau et al. 2020; London 2005) found water concentrations higher than the bulk water concentration in the vicinity of crystals. It is however important to stress that we are not referencing the same process. Indeed, the diffuse interface theory describes nucleus growth on the nanometre scale, and the interfacial water content denotes the water content at the interface of the nucleus during this pre-growth step of the crystallization

process. Contrastingly, Devineau et al. (2020) and London (2005) discussed the water content adjacent to crystals that are orders of magnitude larger than crystal nuclei.

4.3 Independent tests of the nucleation delay model with previous experiments

As a test of the nucleation delay model, we applied our calculations to previous crystallization studies performed on felsic melts. We modelled the nucleation delay times for the experiments of Whitney (1975) and Evensen (2001), both of whom performed experiments on simplified granitic compositions in the $KAlSi_3O_8$-$NaAlSi_3O_8$-$CaAl_2Si_2O_8$-SiO_2 system.

Although Whitney's (1975) data for crystal nucleation from a melt with 4 ± 1 wt% water are very limited, we show good agreement between the theoretical nucleation curve and the experimental data when considering an interfacial water content of 0.9 ± 0.3 wt% (Fig. 12). This interfacial water content is higher than ours and that used by Rusiecka et al. (2020) even though the bulk water concentration of these three studies are similar. However, Whitney performed no experiments at short durations and therefore it is not possible to properly constrain the nucleation curve, which is reflected in the larger range of uncertainty in the interfacial water content. The lower range of 0.6 wt% was selected because it was the smallest water concentration still yielding positive durations and is similar to the value used for quartz and feldspar in this study, and in Rusiecka et al. (2020). This range of interfacial water content, from 0.6 to 1.2 wt%, results in a difference of two order of magnitude in nucleation delays.

For Evensen's (2001) nucleation measurements at water-saturated conditions (7.81 wt% water), the agreement is intermediate, with the highest level of agreement between the theoretical and experimental data reached with an interfacial water content of 1 ± 0.5 wt% (Fig. 13). Only five crystal-free experiments plot within the durations where nucleation is expected by our model

and one crystal-bearing experiment plots at significantly shorter durations than predicted. Nonetheless, most of the crystal-free and crystal-bearing experiments are consistent with our application of the nucleation delay model. Similar to the Mt. Mica experiments, we attribute the few discrepancies between the model and Evensen's experiments to the lack of observations of crystals in crystal-free experiments and the stochastic nature of the nucleation process. Moreover, it is not possible to comment on the individual levels of agreement between theory and experiment for quartz and feldspar since the author did not systematically differentiate between the two phases in his study.

Although Sirbescu et al. (2017) provided detailed crystal nucleation measurements, the melt composition they used was enriched in lithium and boron. Unfortunately, these components are not included in the MELTS software used to estimate the ΔG of formation of the crystalline phases and therefore, it was not possible to accurately model nucleation delay for their specific composition.

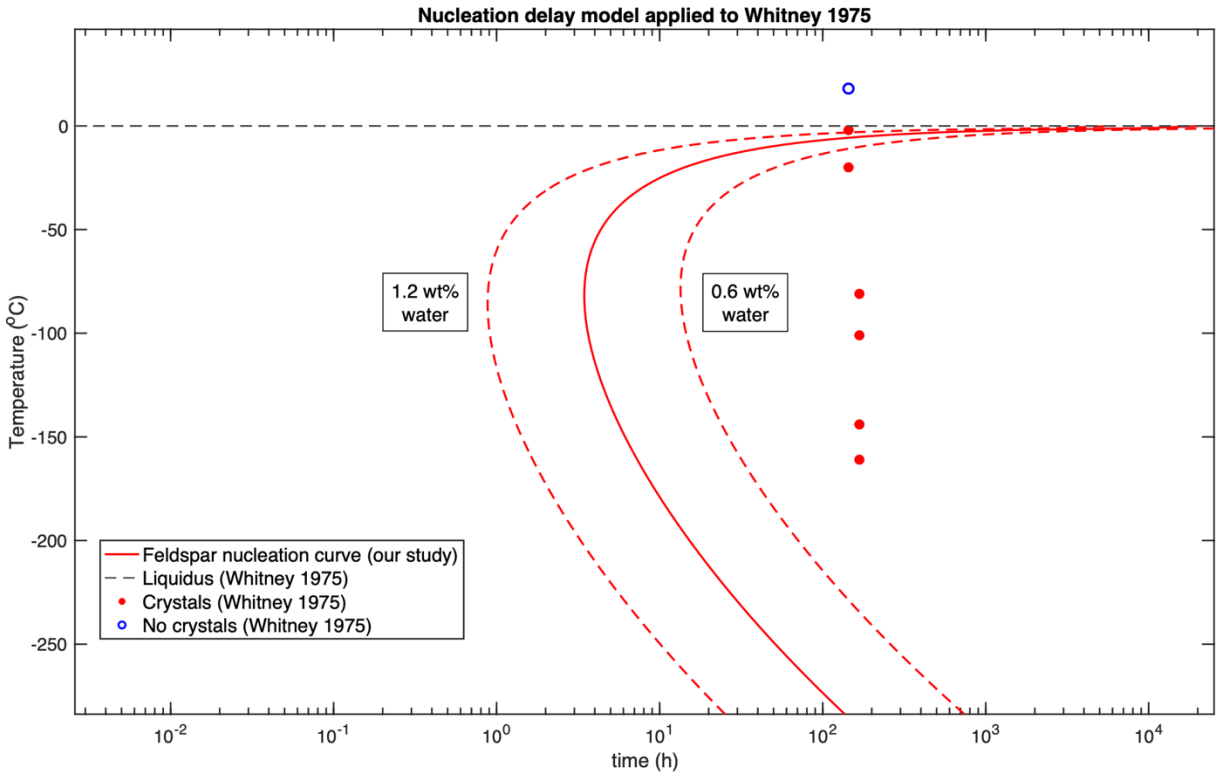

Figure 12. Modelled nucleation delay of feldspar applied to a simplified granitic compositions in the $KAlSi_3O_8$-$NaAlSi_3O_8$-$CaAl_2Si_2O_8$-SiO_2 system. Experimental data from Whitney (1975) at 200 MPa. The water concentration used for the calculation of the activation energy and the interfacial energy is 0.9 $\pm$ 0.3 wt%. Heterogeneous nucleation with a wetting angle of 89 ° was assumed.

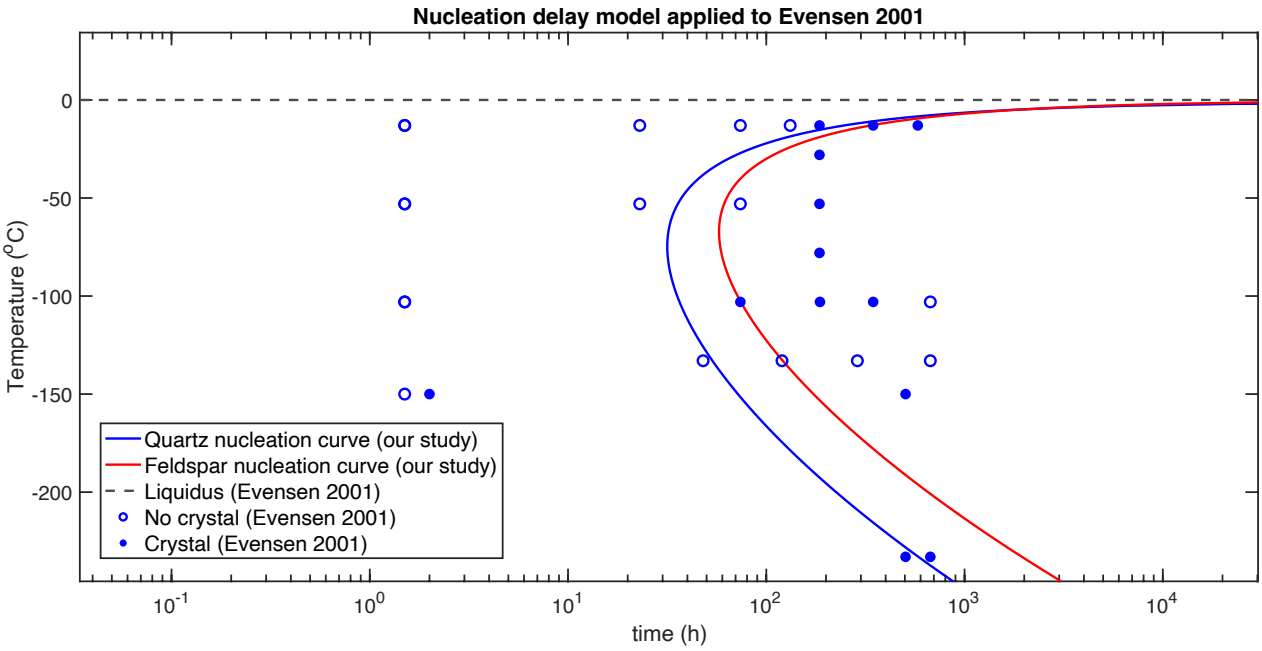

Figure 13. Modelled nucleation delay of feldspar and quartz applied to a simplified granitic compositions in the $KAlSi_3O_8$-$NaAlSi_3O_8$-$CaAl_2Si_2O_8$-SiO_2 system. Experimental data from Evensen (2001) at 200 MPa. The water concentration used for the calculation of the activation energy and the interfacial energy is 1 $\pm$ 0.5 wt%. Heterogeneous nucleation with a wetting angle of 89 ° was assumed.

4.3 Presence of sillimanite and corundum and comparison with the natural rocks of Mt. Mica

Simmon's et al.'s (2016) report on the natural pegmatite from Mt. Mica describes an outer zone composed of albite, quartz, muscovite and schorl and a core zone composed of quartz, albite, microcline, schorl and local pods of rarer minerals (e.g., lepidotite, elbaite, spodumene, pollucite, cassiterite, columbite-group and rare-beryl). There are also garnet and schorl layers occurring

along the footwall portion of the intrusion (Simmons et al. 2016). Noticeably, the mineral assemblage is lacking sillimanite and corundum in the natural rock, unlike the results of our experimental study. Although the goal of this study was not to reproduce the paragenetic sequence of the Mt. Mica pegmatite, these observations demand consideration of the processes possibly responsible for the striking difference in mineralogy between the natural rock and the experimental run products.

A possible explanation for the presence of corundum and sillimanite in the experiments and its absence in the Mt. Mica pegmatite is the possibility of reaction relationships that remove these alumina-rich minerals from the crystallizing assemblage. First, during cooling, corundum could react to produce feldspar and sillimanite, in analogy to the reaction between corundum and the melt to produce mullite ($3Al_2O_3$ - $2SiO_2$) in the Na_2O - SiO_2 - Al_2O_3 system (Lambotte and Chartrand, 2013) or described experimentally by Holtz et al. (1992a, b) in an alumina-rich, haplogranitic system. The presence of crystalline halos surrounding the corundum in our experiments at temperatures lower than 850 °C could possibly be the corundum reacting with the melt to produce a new crystal. These crystalline halos are qualitatively richer in sodium and silicon, and poorer in aluminum and oxygen than the corundum at the center, which could represent an intermediate composition between the melt and the now unstable corundum. Moreover, our melting experiments appear to display replacement textures, with sillimanite crystals following the outline of larger-scale crystals and showing strikingly resemblance to mullite needles replacing early corundum crystals, as seen by Holtz et al. (1992a).

Then, after corundum reacted out, sillimanite could react out of the melt at even lower temperatures. Because there is a large overlap between the sillimanite stability field and

peraluminous felsic melts, magmatic sillimanite is not a petrogenetic riddle and is found in some granitic rocks (e.g., Anderson 1928; Clarke et al. 2005; Villaseca et al. 2012). Equilibrium between a peraluminous granitic melt and sillimanite is consistent with our experiments in which sillimanite displays euhedral crystals, and, unlike corundum, there is no evidence of reaction halos around sillimanite.

The presence of sillimanite in natural granites is associated with earlier period of crystallization at high temperatures and low water activity (D'Amico et al. 1981; Clarke et al. 2005), similar to the experimental conditions in our study. Clarke et al. (2005) proposed that as temperature decreases after high-temperature crystallization the system approaches the supra-liquidus reaction:

$$\text{Orthoclase} + Al_2SiO_5 + \text{Vapour} = \text{Muscovite} + \text{Quartz}, \quad (8)$$

where this reaction could consume the aluminosilicate phase. Therefore, the sillimanite that nucleated at high temperature in our experiments could be consumed by the reaction at lower temperature producing muscovite (Clarke et al. 1976; D'Amico et al. 1981) in the natural rocks of the Mt. Mica pegmatite.

Another possible reaction that could remove sillimanite from the crystallizing assemblage is that at lower temperature, sillimanite could undergo the following reaction (Vielzeuf and Holloway 1988):

$$Al_2SiO_5 + \text{Melt} = \text{Muscovite} + H_2O + \text{Quartz} + \text{Plagioclase} \quad (4)$$

to remove sillimanite and produce muscovite, plagioclase, and quartz, which are abundant in the rocks of Mt. Mica. However, this implies that the melt and the sillimanite react together to form

quartz and feldspar. The sillimanite crystals were euhedral and displayed sharp boundaries with the melt and do not appear to be reacting out of the melt but, the order of crystallization inferred from the crystal relationships (i.e, sillimanite crystals being surrounded by quartz and feldspar) would coincide with this reaction. The unknown phase crystallizing as spherulites does not appear to be a reaction texture as they crystallized homogeneously and heterogeneously on the capsule wall, around corundum crystals or around sillimanite crystals and appear to follow the growth stages of the spherulites as described by Gránásy et al. (2005).

The most probable reason that may explain the absence of sillimanite in the natural pegmatite is that because Mt. Mica crystallized at low pressures (300 MPa) and undercooled conditions (Fig. 14, and Simmons et al. 2016), it possible that sillimanite never crystallized as the intrusion's conditions are in the stability field of muscovite and quartz (Fig. 14).

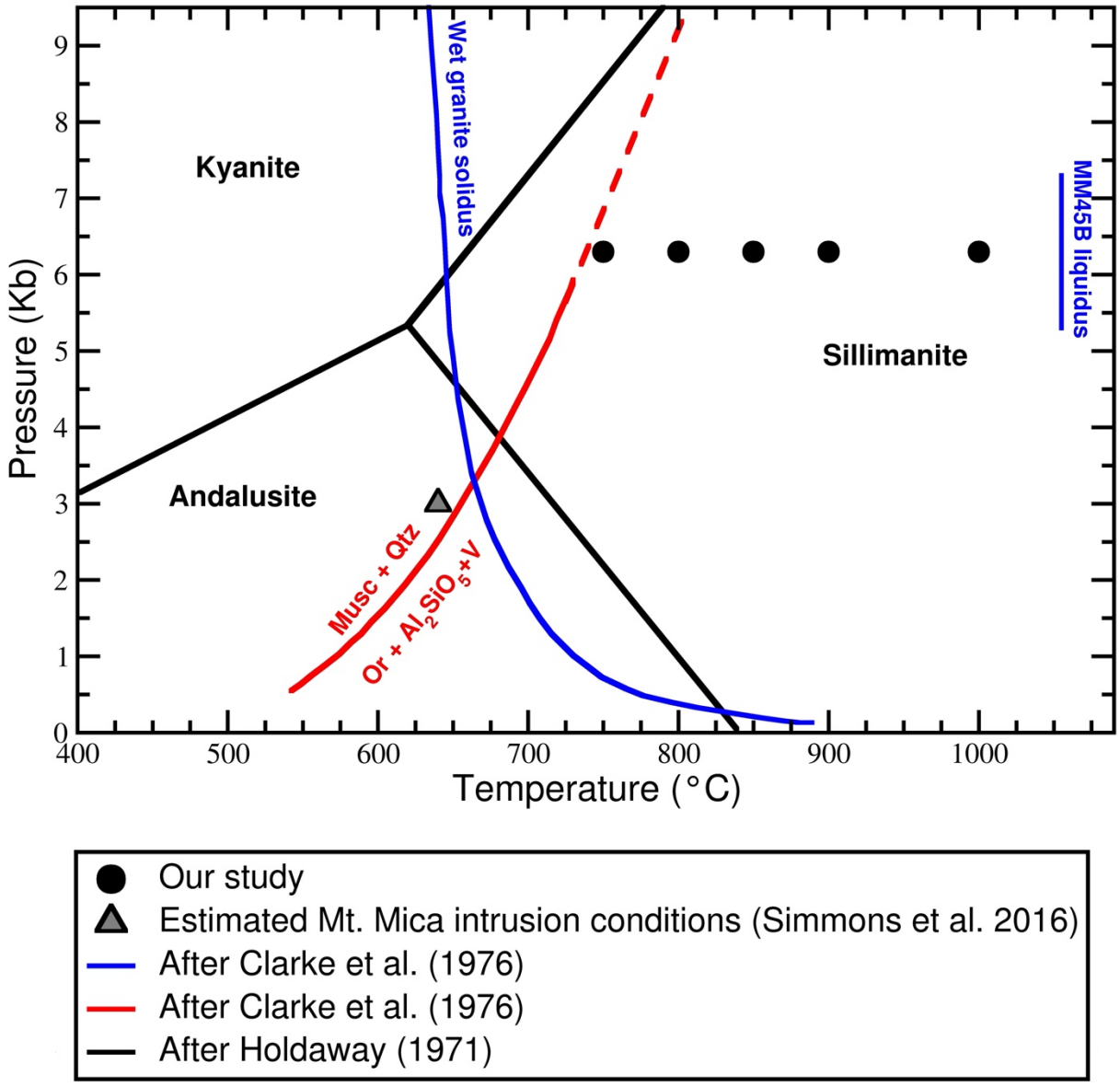

Figure 14. Comparison of experimental temperature and pressure to the Mt. Mica intrusive conditions. Our experiments were performed within the sillimanite stability field. The estimated Mt. Mica intrusive conditions (temperature and pressure) are situated below the Orthoclase + Al_2SiO_5 + V = Muscovite + Quartz reaction. This is therefore a possible explanation as for why the crystallization experiments nucleated sillimanite while the Mt. Mica natural rock is lacking sillimanite.

4.4 Crystal habits: experimental results versus natural pegmatites

Sillimanite and corundum morphological evolution with the degree of undercooling has not been thoroughly studied. Our study therefore presents new data in this field. For sillimanite, we do not see a systematic change in crystal morphology and size as the degree of undercooling or duration of experiments increase. It can, at most, be noted that hollow crystals are observed at intermediate degrees of undercooling (ΔT between -205 and -155) and durations longer than 28 hours. For corundum, intermediate and low degrees of undercooling (ΔT < -205 °C) and durations longer than 28 hours are associated with a euhedral acicular habit while higher degrees of undercooling (ΔT> -205 °C) are associated with the presence of crystalline halos surrounding corundum crystals in the majority of the experiments. There is not a systematic change in corundum and sillimanite crystal size with variation in degrees of undercooling or duration. The change in morphology in these aluminum-rich phases indicate that they are most likely not resulting from quenching our experiments. Similarly, the crystalline halos surrounding corundum occur only in specific experiments at temperatures below 850 °C. If these halos were quench textures, they would be present in all (or at least the majority) of our experiments, which is not what we observed. They are therefore also most likely not resulting from quenching.

Quartz crystal morphologies in our study are consistent with quartz nucleating in other crystallization experiments performed on felsic melts, namely Swanson (1977), Sirbescu et al. (2017), Rusiecka et al. (2020) and Devineau et al. (2020). Quartz displays both anhedral and hexagonal euhedral habits.

For feldspar, spherulites and skeletal crystals coexist in our one feldspar-bearing run product. Past crystallization studies (e.g., Lofgren 1974; Fenn 1977; Swanson 1977; Rusiecka et

al. 2020; Devineau et al. 2020) describe a gradual evolution in the feldspar crystal morphology with increasing degree of undercooling, from tabular crystals, to acicular and skeletal crystals, to various forms of spherulites. This transition from one morphology to another is progressive and more than one crystal habit can coexist in one experimental run product (Lofgren 1974; Swanson 1977), as in ours. The exact degree of undercooling associated with each crystal morphology will vary with the melt composition (Lofgren 1974). However, it is interesting to note that the first morphology in which feldspar crystallized is spherulitic in our study and that, despite having a bulk rock liquidus ~ 300 °C above the feldspar saturation temperature (due to the presence of sillimanite and corundum), the spherulites form within the same range of undercooling below the liquidus (ΔT greater than -200°C) (Lofgren 1974; Fenn 1977; Rusiecka 2020).

Pegmatitic textures (i.e., quartz-feldspar graphic intergrowths), were not produced in this study. However, previous studies that describe such textures (e.g., Maneta and Baker 2014; Sirbescu et al. 2017; Rusiecka et al. 2020; Devineau et al. 2020) denote the presence of graphic intergrowths at lower temperatures (below 650 °C) than our experimental conditions, despite forming at similar range of undercooling than our experimental run conditions (ΔT ranging between -50 and -200 °C). Similarly, we did not observe unidirectional growth analogous to pegmatitic zones as described by Sirbescu et al. (2017) and London and Morgan (2017), but that could be due to the low percent crystallization produced in our experiments.

5. CONCLUDING REMARKS

Crystallization experiments were performed on a hydrous peraluminous melt with a 4.25 wt% water at 630 MPa at temperatures ranging between 750 and 1000 °C. These experiments were compared to a modified theoretical nucleation delay model based on the classical nucleation theory (CNT). The model was also applied to nucleation delay data in felsic melts available in the literature. Despite various crystallization studies being carried out in the last half century, there is still a significant gap in the literature and, before 5 years ago, little to no work has been done on applying theoretical models to nucleation delay in natural magmatic composition. This gap in quantifiable nucleation delay data is especially present when investigating natural and complex granitic melts. This study is therefore a stepping stone in further constraining nucleation delay timescales in felsic melts.

Considering each of the studies to which we apply the modified CNT model (including ours), we can see that the model shows relatively good agreement with the experimental data at granite crystallization temperatures below 900 °C. Within this range of temperature, sillimanite and corundum experimental results show a good agreement (within a factor of 2) with their theoretical nucleation curves. Without considering Evensen (2001) due to the lack of specific separated data on quartz and feldspar nucleation, the theoretical nucleation curves accurately describes the nucleation delay of quartz, while feldspar shows, at worst, an agreement factor of 5. Even if the level of agreement is not perfect, we demonstrate that within at least an order of magnitude, the model can provide good estimates of the timescales of nucleation delay within felsic melts. However, more data would be required to improve the constraints of quartz and feldspar nucleation delay at higher degrees of undercooling, especially when discussing the formation of pegmatitic textures. Nevertheless, this study shows that this model provides

promising estimates on nucleation delay, regardless of the melt composition and phase studied, further supporting the findings of Rusiecka et al. (2020).

REFERENCES

Abramoff, M.D., Magalhaes, P.J., and Ram, S.J. (2004). Image processing with ImageJ: Biophotonics International, v. 11, no. 7, p. 36–42.

Anderson, A.L. (1928). Genesis of the Silver Hill Tin Deposits: The Journal of Geology, v. 36, no. 7, p. 646–664, doi: 10.1086/623563.

Arzilli, F., Stabile, P., Fabbrizio, A., Landi, P., Scaillet, B., Paris, E., and Carroll, M.R. (2020). Crystallization kinetics of alkali feldspar in peralkaline rhyolitic melts: Implications for pantelleria volcano: Frontiers in Earth Science, v. 8, doi: 10.3389/feart.2020.00177.

Baker, D.R. (1990). Chemical interdiffusion of dacite and rhyolite: anhydrous measurements at 1 atm and 10 kbar, application of transition state theory, and diffusion in zoned magma chambers. Contributions to Mineralogy and Petrology, 104, 407–423.

Baker, D. R. (1992). Estimation of diffusion coefficients during interdiffusion of geologic melts: application of transition state theory. Chemical Geology, 98, 11-21. https://doi.org/10.1016/0009-2541(92)90089-N

Baker, D.R., and Freda, A. (2001). Eutectic crystallization in the undercooled orthoclase-quartz-H2O system: Experiments and simulations: European Journal of Mineralogy, v. 13, no. 3, p. 453–466, doi: 10.1127/0935-1221/2001/0013-0453.

Behrens, H., Roux, J., Neuville, D.R., Siemann, M. (2006). Quantification of dissolved H_2O in silicate glasses using confocal microRaman spectroscopy. Chemical Geology, 229, 96-112.

Berkebile, C.A., Dowty, E. (1982). Nucleation in laboratory charges of basaltic composition. American Mineralogist, 67, 886-899.

Bowen, N.L. (1913). The melting phenomena of the plagioclase feldspars: American Journal of Science, v. s4-35, no. 210, p. 577–599, doi: 10.2475/ajs.s4-35.210.577.

Collins, F. C. (1955). Time lag in spontaneous nucleation due to non-steady state effects. Zeitschrift für Elektrochemie, Berichte der Bunsengesellschaft für physikalische Chemie, 59, 404-409.

Černý, P. (1991). Rare-element Granitic Pegmatites. Part I: Anatomy and Internal Evolution of Pegmatitic Deposits. Geoscience Canada, 18.

Clarke, D., Dorais, M., Barbarin, B., Barker, D., Cesare, B., Clarke, G., El Baghdadi, M., Erdmann, S., Förster, H.-J., Gaeta, M., Gottesmann, B., Jamieson, R., Kontak, D., Koller, F., et al. (2005). Occurrence and origin of andalusite in peraluminous felsic igneous rocks: Journal of Petrology, v. 46, no. 3, p. 441–472, doi: 10.1093/petrology/egh083.

Clarke, D.B., McKenzie, C.B., Muecke, G.K., and Richardson, S.W. (1976). Magmatic andalusite from the South Mountain Batholith, Nova Scotia: Contributions to Mineralogy and Petrology, v. 56, no. 3, p. 279–287, doi: 10.1007/bf00466826.

Couch, S. (2003). The kinetics of degassing-induced crystallization at Soufriere Hills volcano, Montserrat: Journal of Petrology, v. 44, no. 8, p. 1477–1502, doi: 10.1093/petrology/44.8.1477.

D'Amico, C., Rottura, A., Maccarrone, E., and Puglisi, G. (1981). Peraluminous granitic suite of Calabria-Peloritani arc (Southern Italy): Società Italiana di Mineralogia e Petrologia, v. 38, no. 1, p. 35–52.

De Yoreo, J.J., Vekilov, P.G. (2003), Principles of crystal nucleation and growth. Reviews in Mineralogy and Geochemistry 54, 57–93.

Devineau, K., Champallier, R., and Pichavant, M. (2020). Dynamic crystallization of a haplogranitic melt: Application to pegmatites: Journal of Petrology, v. 61, no. 5, doi: 10.1093/petrology/egaa054.

Donaldson, C. H. (1979). An experimental investigation of the delay in nucleation of olivine in mafic magmas. Contributions to Mineralogy and Petrology, 69, 21-32.

Evensen, J.M. (2001). The geochemical budget of beryllium in silicic melts and superliquidus, subliquidus and starting state effects on the kinetics : University of Oklahoma.

Fenn, P.M. (1977). The nucleation and growth of alkali feldspars from hydrous melts: The Canadian Mineralogist, v. 15, p. 135–161.

Fortin, M-A., Riddle, J., Desjardins-Langlais, Y., Baker, D.R. (2015). The effect of water on the sulfur concentration at sulfide saturation (SCSS) in natural melts. Geochimica et Cosmochimica Acta, 160, 100-116.

Fokin, V.M., Zanotto, E.D., Yuritsyn, N.S., and Schmelzer, J.W. (2006). Homogeneous crystal nucleation in silicate glasses: A 40 years perspective. Journal of Non-Crystalline Solids, 352, 2681–2714.

Gibbs, J.W. (1875–1878). On the Equilibrium of Heterogeneous Substances. Transactions of the Connecticut Academy of Arts Sciences, 108, 343.

Gibb, E. G. E. (1974). Supercooling and the crystallization of plagioclase from a basaltic magma. Mineralogical Magazine, 39, 641-653.

Ghiorso, M.S., and Sack, R.O. (1995). Chemical mass transfer in magmatic processes IV. A revised and internally consistent thermodynamic model for the interpolation and extrapolation of liquid-solid equilibria in magmatic systems at elevated temperatures and pressures. Contributions to Mineralogy and Petrology, 119, 197–212.

Gránásy, L. (1993). Diffuse interface approach to vapour condensation. Europhysics Letters, 24, 121-126. https://doi.org/10.1209/0295-5075/24/2/008.

Gránásy, L. (1996). Fundamentals of the diffuse interface theory of nucleation. The journal of physical chemistry, 100, 10768-10770. https://doi.org/10.1021/jp953695c

Gránásy, L., Pusztai, T., Tegze, G., Warren, J.A., and Douglas, J.F. (2005). Growth and form of Spherulites: Physical Review E, v. 72, no. 1, doi: 10.1103/physreve.72.011605.

Gualda, G.A.R., Ghiorso, M.S., Lemons, R.V., and Carley, T.L. (2012). Rhyolite-MELTS: a Modified Calibration of MELTS Optimized for Silica-rich, Fluid-bearing Magmatic Systems. Journal of Petrology, 53, 875–890.

Gutzov, I., and Schmelzer, J. W. P. (1995). The vitreous state: thermodynamics, structure, rheology, and crystallization. Springer.

Hammer, J.E. (2004). Crystal nucleation in hydrous rhyolite: Experimental data applied to classical theory. American Mineralogist, 89, 1673–1679.

Hammer, J.E. (2008). Experimental Studies of the Kinetics and Energetics of Magma Crystallization. Reviews in Mineralogy and Geochemistry, 69, 9–59.

Holdaway, M.J. (1971). Stability of andalusite and the aluminum silicate phase diagram: American Journal of Science, v. 271, no. 2, p. 97–131, doi: 10.2475/ajs.271.2.97.

Holtz, F., Johannes, W., and Pichavant, M. (1992a). Effect of excess aluminium on phase relations in the system Qz-Ab-Or: Experimental investigation at 2 KBAR and reduced H2O-activity: European Journal of Mineralogy, v. 4, no. 1, p. 137–152, doi: 10.1127/ejm/4/1/0137.

Holtz, F., Johannes, W., and Pichavant, M. (1992b). Peraluminous granites: The effect of alumina on melt composition and coexisting minerals: Geological Society of America Special Papers, p. 409–416, doi: 10.1130/spe272-p409.

Jahns, R.H., and Burnham, C.W. (1969). Experimental studies of pegmatite genesis: a model for the derivation and crystallization of granitic pegmatites: Economic Geology, v. 64, no. 8, p. 843–864, doi: 10.2113/gsecongeo.64.8.843.

Kalikmanov, V.I. (2013). Nucleation theory: Springer Netherlands, Dordrecht.

Kashchiev, D (1969). Solution of the non-steady state problem in nucleation kinetics. Surface Science 14:209–220.

Kashchiev, D. (2000). Nucleation: Basic theory with applications: Butterworth Heinemann, Oxford.

Kirkpatrick, R.J. (1981). Kinetics of crystallization of igneous rocks. Reviews in Mineralogy, 8.

Lambotte, G., and Chartrand, P. (2013). Thermodynamic modeling of the (Al_2O_3+Na_2O), (Al_2O_3+ Na_2O +SiO_2), and (Al_2O + Na_2O +AlF_3+NaF) systems, The Journal of Chemical Thermodynamics, 57, 306–334.

Linnen R.L., Van Lichtervelde M., Černý P. (2012). Granitic pegmatites as sources of strategic metals. Elements 8:275–280. doi: 10.2113/gselements.8.4.275

Lofgren, G. (1974). An experimental study of plagioclase crystal morphology; isothermal crystallization: American Journal of Science, v. 274, no. 3, p. 243–273, doi: 10.2475/ajs.274.3.243.

London, D. (2005). Granitic pegmatites: an assessment of current concepts and directions for the future. Lithos, 80, 281–303.

London, D. (2008). Pegmatites: Mineralogical Association of Canada, Québec

London, D. (2018). Ore-forming processes within granitic pegmatites: Ore Geology Reviews, v. 101, p. 349–383, doi: 10.1016/j.oregeorev.2018.04.020.

London, D. (2023). An experimental crystallization of the Macusani obsidian in a thermal gradient with applications to lithium-rich granitic pegmatites: American Mineralogist, doi: 10.2138/am-2022-8674.

London, D., and Morgan, G.B. (2017). Experimental crystallization of the Macusani Obsidian, with applications to lithium-rich granitic pegmatites: Journal of Petrology, v. 58, no. 5, p. 1005–1030, doi: 10.1093/petrology/egx044.

London, D., Morgan, G.B., and Hervig, R.L. (1989). Vapor-undersaturated experiments with Macusani Glass+H2O at 200 MPA, and the internal differentiation of granitic pegmatites: Contributions to Mineralogy and Petrology, v. 102, no. 1, p. 1–17, doi: 10.1007/bf01160186.

London, D., Wolf, M.B., Morgan, G.B., and Garrido, M.G. (1999). Experimental silicate-phosphate equilibria in peraluminous granitic magmas, with a case study of the Alburquerque Batholith at Tres Arroyos, Badajoz, Spain: Journal of Petrology, v. 40, no. 1, p. 215–240, doi: 10.1093/petroj/40.1.215.

Maaløe, S., and Wyllie, P.J. (1975). Water content of a granite magma deduced from the sequence of crystallization determined experimentally with water-undersaturated conditions: Contributions to Mineralogy and Petrology, v. 52, no. 3, p. 175–191, doi: 10.1007/bf00457293.

Maneta, V., and Baker, D.R. (2014). Exploring the effect of lithium on pegmatitic textures: An experimental study: American Mineralogist, v. 99, no. 7, p. 1383–1403, doi: 10.2138/am.2014.4556.

Mazzotti, M., Vetter, T., Ochsenbein, D.R., Maggioni, G.M., and Lindenberg, C. (2018). Nucleation: Polymorphism in the Pharmaceutical Industry, p. 261–283, doi: 10.1002/9783527697847.ch9.

Mollard, E., Martel, C., and Bourdier, J.-L. (2012). Decompression-induced crystallization in hydrated silica-rich melts: Empirical models of experimental plagioclase nucleation and growth kinetics: Journal of Petrology, v. 53, no. 8, p. 1743–1766, doi: 10.1093/petrology/egs031.

Nabelek, P.I., Whittington, A.G., and Sirbescu, M.-L.C. (2010). The role of H2O in rapid emplacement and crystallization of granite pegmatites: Resolving the paradox of large crystals in highly undercooled melts: Contributions to Mineralogy and Petrology, v. 160, no. 3, p. 313–325, doi: 10.1007/s00410-009-0479-1.

Naney, M.T., and Swanson, S.E. (1980). The effect of Fe and Mg on crystallization in granitic systems. American Mineralogist, 65, 639–653.

Neuville, D.R., Cornier, L., Caurant, D., and Montagne, L. (2020). From glass to Crystal: Nucleation, growth and phase separation: From research to applications: EDP Sciences, Les Ulis.

Rossman, G. R. (1996). Studies of oh in nominally anhydrous minerals. Physics and Chemistry of Minerals, 23(4-5). https://doi.org/10.1007/bf00207777

Rusiecka, M.K., and Baker, D.R. (2021). Growth and textural evolution during crystallization of quartz and feldspar in hydrous, rhyolitic melt: Contributions to Mineralogy and Petrology, v. 176, no. 7, doi: 10.1007/s00410-021-01809-1.

Rusiecka, M.K., Bilodeau, M., and Baker, D.R. (2020). Quantification of nucleation delay in magmatic systems: experimental and theoretical approach. Contributions to Mineralogy and Petrology, 175.

Rusiecka, M.K., and Martel, C. (2022). Nucleation delay in water-saturated rhyolite during decompression in shallow volcanic systems and its implications for ascent dynamics: Bulletin of Volcanology, v. 84, no. 6, doi: 10.1007/s00445-022-01569-1.

Schmelzer, J. W. P. (2008). Crystal nucleation and growth in glass-forming melts: Experiment and theory. Journal of Non-Crystalline Solids, 354, 269-278.

Schneider, C.A., Rasband, W.S., and Eliceiri, K.W. (2012). NIH image to imagej: 25 years of image analysis: Nature Methods, v. 9, no. 7, p. 671–675, doi: 10.1038/nmeth.2089.

Shannon R.D. (1976). Revised effective onic radii and systematic studies of interatomic distances in halides and chalcogenides. Acta Crystallographica Section A 32:751–767.

Simmons, W., Falster, A., Webber, K., Roda-Robles, E., Boudreaux, A.P., Grassi, L.R., and Freeman, G. (2016). Bulk Composition of Mt. Mica Pegmatite, Maine, USA: Implications for the Origin of an Lct Type Pegmatite by Anatexis. The Canadian Mineralogist, 54, 1053–1070.

Simmons, W.B.S., and Webber, K.L. (2008). Pegmatite genesis: state of the art. European Journal of Mineralogy, 20, 421–438.

Sirbescu, M.-L.C., Doran, K., Konieczka, V.A., Brennan, C.J., Kelly, N.M., Hill, T., Knapp, J., and Student, J.J. (2023). Trace element geochemistry of spodumene megacrystals: A combined portable-XRF and micro-XRF study: Chemical Geology, v. 621, p. 121371, doi: 10.1016/j.chemgeo.2023.121371.

Sirbescu, M.-L.C., Schmidt, C., Veksler, I.V., Whittington, A.G., and Wilke, M. (2017). Experimental crystallization of undercooled felsic liquids: Generation of Pegmatitic texture: Journal of Petrology, v. 58, no. 3, p. 539–568, doi: 10.1093/petrology/egx027.

Slezov, V.V. and Schmelzer, J.W.P., (1999). Kinetics of nucleation–growth processes: the first

stages. In: Schmelzer, J. W. P., Röpke, G., Priezzhev, V. B. (Eds.) Nucleation Theory and Applications, pp.6-81.

Swanson, S.E. (1977). Relation of nucleation and crystal-growth rate to the development of granitic textures. American Mineralogist, 62, 966–978.

Turnbull, D., Fisher, J. C. (1949). Rate of nucleation in condensed systems. The Journal of chemical physics, 17, 71-73. doi: 10.1063/1.1747055.

Vielzeuf D, Holloway J.R. (1988). Experimental determination of the fluid-absent melting relations in the pelitic system. Contributions to Mineralogy and Petrology 98:257–276.

Villaseca, C., Pérez-Soba, C., Merino, E., Orejana, D., López-García, J.A., and Billstrom, K. (2012). Contrasted crustal sources for peraluminous granites of the segmented Montes de Toledo batholith (Iberian variscan belt): Journal of GEOsciences, p. 263–280, doi: 10.3190/jgeosci.035.

Webber, K.L., Simmons, W.B., Falster, A.U., and Foord, E.E. (1999). Cooling rates and crystallization dynamics of shallow level pegmatite-aplite dikes, San Diego County, California: American Mineralogist, v. 84, no. 5-6, p. 708–717, doi: 10.2138/am-1999-5-602.

Wilke, S., Holtz, F., Neave, D.A., and Almeev, R. (2017). The effect of anorthite content and water on quartz–feldspar cotectic compositions in the rhyolitic system and implications for geobarometry: Journal of Petrology, v. 58, no. 4, p. 789–818, doi: 10.1093/petrology/egx034.

White, W.M. (2013) Geochemistry. Wiley Blackwell, Chichester.

Whitney, J.A. (1975). The Effects of Pressure, Temperature, and XH2O on Phase Assemblage in Four Synthetic Rock Compositions. The Journal of Geology, 83, 1–31.

APPENDIX 1. Sillimanite and corundum crystal morphology and textures produced in the crystallization experiments

Sillimanite crystal morphologies and textures evolution in the studied range of temperature and run duration for the crystallization experiments

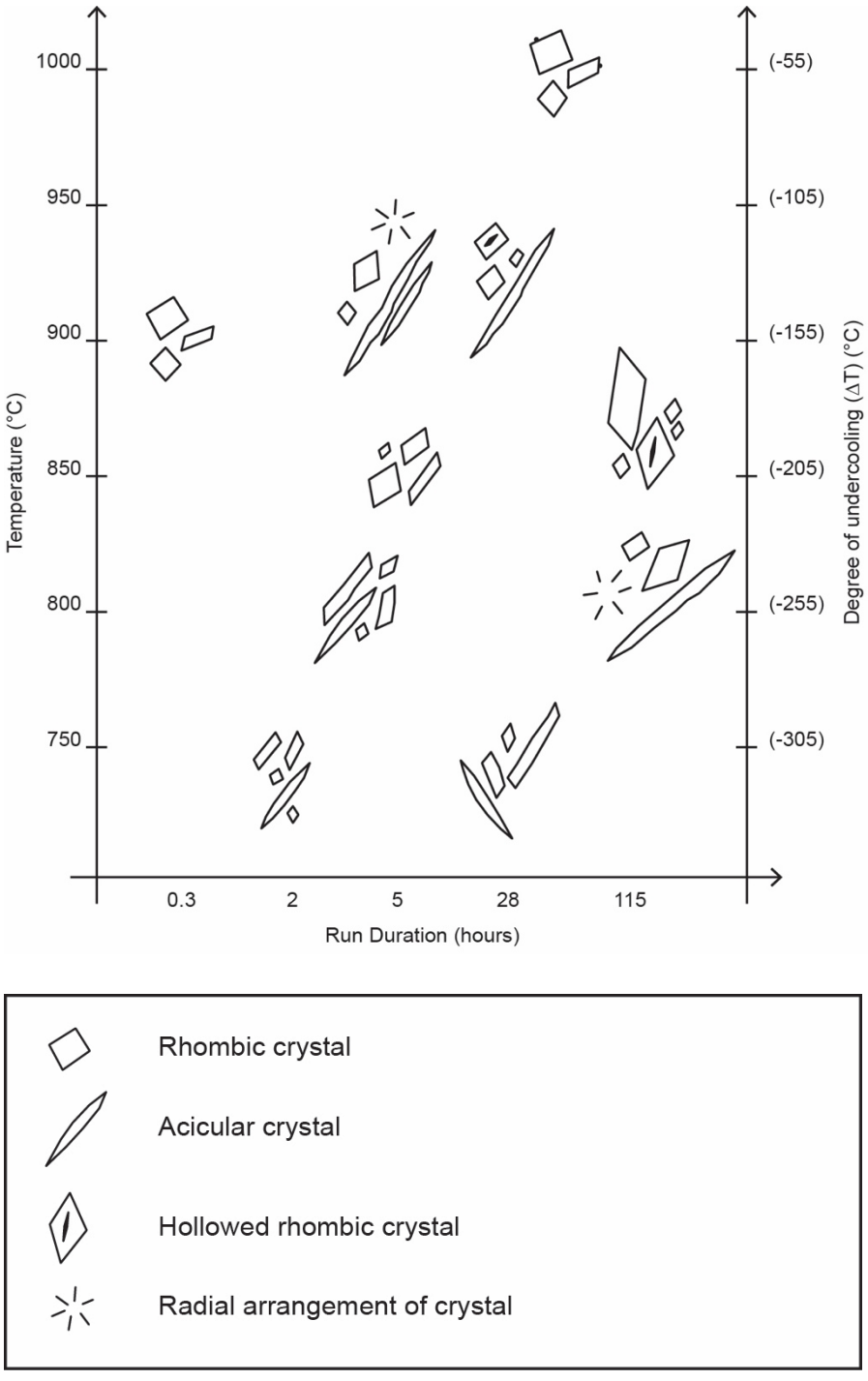

Corundum crystal morphologies and textures evolution in the studied range of temperature and run duration for the crystallization experiments.

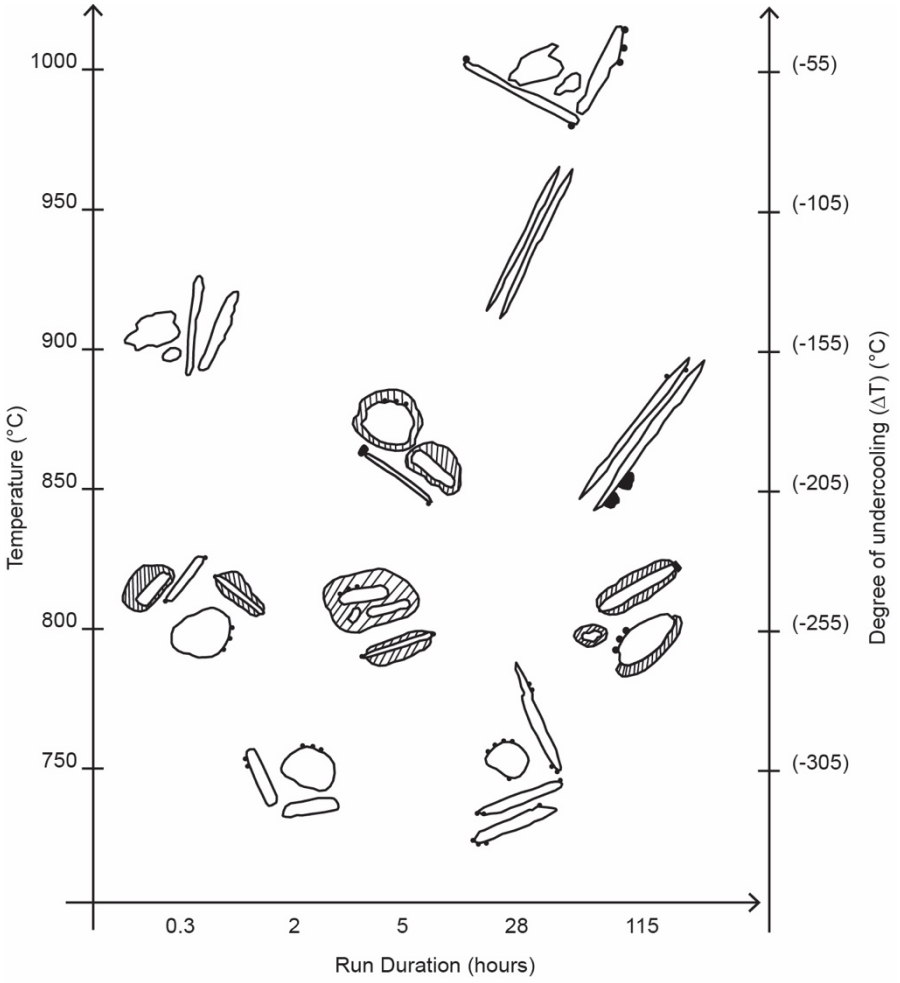

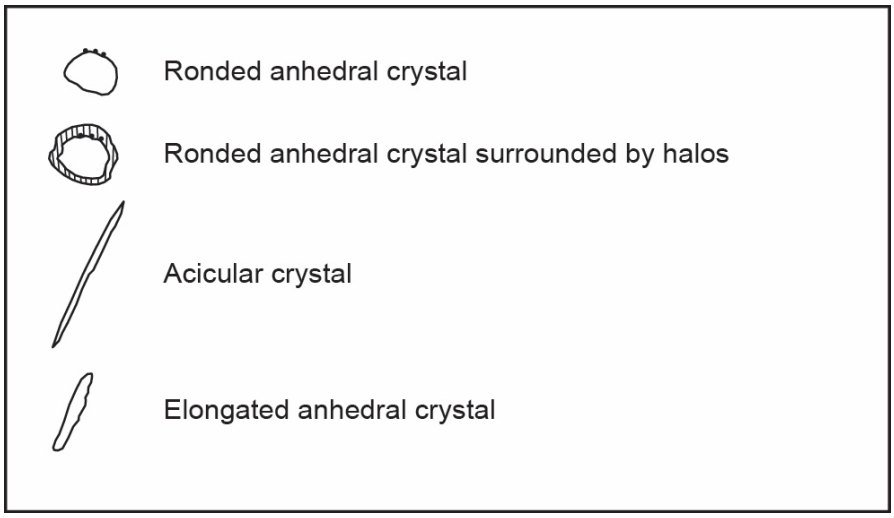

APPENDIX 2. Representative crystal composition in melting experiments

Oxide	Sillimanite composition (wt%)	Corundum composition (wt%)	Quartz composition (wt%)	Feldspar composition (wt%)
SiO_2	50.0109 (15.0266)	13.0681 (5.7574)	95.4063 (2.8699)	72.7203 (4.3747
Al_2O_3	44.6534 (16.5996)	84.0208 (5.56481)	3.7497 (2.3230)	18.1392 (1.6868)
CaO	0.1526 (0.1411)	0.0216 (0.0315)	0.0296 (0.0409)	1.0780 (0.3856)
Na_2O	1.7756 (1.0149)	0.5216 (0.3658)	0.4766 (0.4497)	7.2656 (2.2499)
K_2O	0.7612 (0.4964)	0.2006 (0.1434)	0.1910 (0.1579)	0.7970 (0.0523)

The average composition was calculated using MATLAB and was based on at least five datapoint from each experiment at the studied temperatures and durations. One standard deviation (showed in parenthesis) was also calculated using MATLAB and shows the dispersion through the dataset of each of the crystal composition.

APPENDIX 3. Modified nucleation delay model based on the classical nucleation theory (CNT)

```
% NucleationDelayGranite.m

%Permission is hereby granted, free of charge, to any person obtaining
%a copy of this software and associated documentation files (the
%√¢¬Ä¬úSoftware√Ø¬ø¬Ω?), to deal in the Software without restriction,
including
%without limitation the rights to use, copy, modify, merge, publish,
%distribute, sublicense, and/or sell copies of the Software, and to
%permit persons to whom the Software is furnished to do so, subject
%to the following conditions:

%The above copyright notice and this permission notice shall be included
%in all copies or substantial portions of the Software.

%THE SOFTWARE IS PROVIDED √¢¬Ä¬úAS IS√Ø¬ø¬Ω?, WITHOUT WARRANTY OF ANY KIND,
%EXPRESS OR IMPLIED, INCLUDING BUT NOT LIMITED TO THE WARRANTIES OF
%MERCHANTABILITY, FITNESS FOR A PARTICULAR PURPOSE AND NONINFRINGEMENT.
%IN NO EVENT SHALL THE AUTHORS OR COPYRIGHT HOLDERS BE LIABLE FOR ANY
%CLAIM, DAMAGES OR OTHER LIABILITY, WHETHER IN AN ACTION OF CONTRACT,
%TORT OR OTHERWISE, ARISING FROM, OUT OF OR IN CONNECTION WITH THE
%SOFTWARE OR THE USE OR OTHER DEALINGS IN THE SOFTWARE.


% Nucleation delay time (tau) calculations base upon several different papers
% written by Don R. Baker, McGill University, January 2018
% Nasciemento et al. equation fixed 22 January 2019
% based upon spreadsheet calculations of 2014


clear all

% constants needed for calculations
Ao=6.022e23; %Avogadro's number
kb=1.380658e-23; % Boltzmann's constant (J/K)
R=8.314510; % gas constant (J/mole K)
h=6.6260755e-34;  %Planck's constant (J s)


%Variables that need to be set for the calculations
sigmanot = 0.2; % 0.12, 0.14, 0.2, 0.33 sometimes used -- surface free energy
(J/m^2)
lambda = 0.26e-10; % diffusion jump distance (m)
% Al3+ ion radius = 0.39e-10
% Si4+ ion radius = 0.26e-10
% Order of magnitude value = 1e-10

%Tolman distance modification to calculate Rc and sigma
% following Abyzov et al. (2017) J. Non-Crystalline Solids
%relative values of delta/lambda vary from 0.4 to 1.6
delta = lambda*0.4; % Tolman equation distance;
```

```
Mqtz = 2.27e-5; %molar volume of quartz (m^3/mol)
Malb = 1.01e-4; %molar volume of albite (m^3/mol)
Morth = 1.08e-4; %molar volume of orthoclase (m^3/mol)
Manth = 1.0079e-4; %molar volume of anorthite(m^3/mol)


% all of the following are with 6 wt% H20 in the melt
%G values calculated using PhasePlot by Mark Ghiorso
% Affinity calculated by phase plot (not allowing crystallization)
% of quartz or feldspars is set equal to G of crystallization
% cuz affinity in PhasePlot is for the melting reaction
% the values of G(J/mol) are divided by the molecular volumes
% to get G in J/m^3


% Composition is LCO with 6 wt% H2O (need to double check composition)
%quartz

Gqtz5005=-3175.52/Mqtz; %DeltaG qtz xtallization 500C,500Mpa
Gqtz5505=-2500.37/Mqtz; %DeltaG qtz xtallization 550C,500Mpa (J/mol)
Gqtz6005=-2037.5/Mqtz; %DeltaG qtz xtallization 600C,500Mpa (J/molz6005=-
2037.5;
Gqtz6505=-1491.29/Mqtz; %DeltaG qtz xtallization 660C,500Mpa (J/molz6005=-
2037.5;

Gqtz5(1) = Gqtz5005;
Gqtz5(2) = Gqtz5505;
Gqtz5(3) = Gqtz6005;
Gqtz5(4) = Gqtz6505;

Gqtz5(5) = -1068.45/Mqtz; % 700 C, extrapolation from data above (not
PlotData)
Gqtz5(6) = -672.65/Mqtz; % 750 C, extrapolation from data above (not
PlotData)
Gqtz5(7) = -313.73/Mqtz; % 800 C, extrapolation from data above (not
PlotData)
Gqtz5(8) = -0.0001/Mqtz; % 850 C, extrapolation from data above (not
PlotData)


Gqtz5002 = -2292.21/Mqtz;%DeltaG qtz xtallization 500C,200Mpa
Gqtz5502 = -1745.48/Mqtz;%DeltaG qtz xtallization 550C,200Mpa
Gqtz6002 = -1219.21/Mqtz;%DeltaG qtz xtallization 600C,200Mpa
Gqtz6502 = -743.5/Mqtz;%DeltaG qtz xtallization 650C,200Mpa


%plagioclase in granitic composition
GPlag5005=-13916.38/Malb; %DeltaG plag xtallization 500C,500Mpa
GPlag5505=-11538.29/Malb; %DeltaG plag xtallization 550C,500Mpa (J/mol)
GPlag6005=-9087.16/Malb; %DeltaG plag xtallization 600C,500Mpa (J/molz6005=-
2037.5;
GPlag6505=-6596.88/Malb; %DeltaG plag xtallization 660C,500Mpa (J/molz6005=-
2037.5;

GPlag5(1) = GPlag5005;
```

```
GPlag5(2) = GPlag5505;
GPlag5(3) = GPlag6005;
GPlag5(4) = GPlag6505;

GPlag5(5) = -5168.30/Malb; % 700 C, extrapolation from data above (not
PlotData)
GPlag5(6) = -3496.92/Malb; % 750 C, extrapolation from data above (not
PlotData)
GPlag5(7) = -1981.32/Malb; % 800 C, extrapolation from data above (not
PlotData)
GPlag5(8) = -600.67/Malb; % 850 C, extrapolation from data above (not
PlotData)



GPlag5002 = -12731.46/Malb;%DeltaG plag xtallization 500C,200Mpa
GPlag5502 = -10334.7/Malb;%DeltaG plag xtallization 550C,200Mpa
GPlag6002 = -7859.8/Malb;%DeltaG plag xtallization 600C,200Mpa
GPlag6502 = -5345.72/Malb;%DeltaG plag xtallization 650C,200Mpa


%*****************Basalic melt diffusion parameters************************
%Plagioclase in Gibb's basalt experiments:
%Supercooling and the crystallization of plagioclase from a basaltic magma
%Mineralogical Magzine 1974
%plagioclase liquidus T from Gibb:  1198 +/- 1 C

%Arrhenius equations for Si tracer diffusion
% in a dry basalt with 48 wt% SiO2 (Lesher et al., 1996 GCA)
% Zhang et al. (2010, Rev Min) use these values as a refernce for basalt

%Nominally dry
DoB = 3.7e-6; %m^2
DoplusB = 4.60e-5;  %positive uncertainty in Do
DominusB = 3.1e-6; % negatative uncertainty in Do
EaB = 170000; % J/mol
DeltaEaB = 2000; % Uncertaintiy in activation energy

%Zhang et al. (2010) Review in Mineralogy

%Nominally dry basalt, fit to Al interdiffusion (Equation 34)

DoAlB = 0.0031828;
EaAlB = 2.6017e5;

% No data in Zhange et al for EBDC Si diffuison in Nominally dry basalt


%************Granitic melt diffusion parameters*****************

%Arrhenius equations for Si-Al interdiffusion
%Dry melts with 70 wt% SiO2 from Baker (1990) Con Min Pet
%Hydrous melts with 70wt% SiO2 from Baker (1991) Con Min Pet

% Nominally dry
```

```
Do = 6.73e-6; %m^2
Doplus = 2.90e-5;  %positive uncertainty in Do
Dominus = 5.46e-6; % negatative uncertainty in Do
Ea = 236400; % J/mol
DeltaEa = 23900; % Uncertaintiy in activation energy

% 3 wt% water in melt

Do3 = 2.58e-8; %m^2
Do3plus = 2.62e-8;  %positive uncertainty in Do
Do3minus = 1.3e-8; % negatative uncertainty in Do
Ea3 = 126500; % J/mol
DeltaEa3 = 8500; % Uncertaintiy in activation energy

% 6 wt% water in melt

Do6 = 2.69e-7; %m^2
Do6plus = 2.35e-3;  %positive uncertainty in Do
Do6minus = 2.69e-7; % negatative uncertainty in Do
Ea6 = 131300; % J/mol
DeltaEa6 = 110500; % Uncertaintiy in activation energy


% Calculations after Nascimento et al. 2011 -- tauN
% Calculations after Fokin et al. 2006 -- tauF

%TC = [500,550,600,650,700,750,800,850];

%fitting DeltaG for Qtz and for Plag in xmgrace and then creating functions

%TC=[400:1:872]; %Temperatures for pegmatites
%TC=[107:1:862]; %Test Temperatures for pegmatites
TC = [400:1:900]; % Mt. Mica, 4 wt$% water, 630 MPa temperatures

%TC =[620:10:1021]; % Temperatures for dry LCO

%TC=[1140:1:1198]; %Temperatures for basalts

TK = 273.15 + TC;
TKinv=1./(TK);

GqtzTest = Gqtz5;
GPlagTest = GPlag5;

%5 kbar
Gqtz6 =  (-7.8794e6.*TKinv +7029.6)/Mqtz; % quartz in granitic melt with 6
wt% water, 5 kbar

GPlag6 = (-3.3273e7.*TKinv +29027)/Malb;  % albite in granitic melt with 6
wt% water, 5 kbar

Gqtz4 =  (-7.9926e6.*TKinv +6917.2)/Mqtz; % quartz in granitic melt with 4
wt% water, 5 kbar
GPlag4 = (-4.1148e7.*TKinv +35641)/Malb;  % albite in granitic melt with 4
wt% water, 5 kbar
```

```
%5.5 kbar calculations added on 9 Sept 2019
Gqtz4_55 = (-10085 + 16.165.*TC - 0.0050518*TC.^2)/Mqtz; % quartz in LCO
granitic melt with 4 wt% water, 6.5 kbar
GPlag4_55 = ( -39404 + 46.446*TC)/Malb; %feldspar in LCO granitic melt with 4
wt% water, 6.5 kbar

%6.0 kbar calculations added on 9 Sept 2019
Gqtz4_60 = (-10249 + 16.223.*TC - 0.0050178*TC.^2)/Mqtz; % quartz in LCO
granitic melt with 4 wt% water, 6.5 kbar
GPlag4_60 = ( -39468 + 46.338*TC)/Malb; %feldspar in LCO granitic melt with 4
wt% water, 6.5 kbar


%6.5 kbar calculations added on 7 Sept 2019
Gqtz4_65 = (-10463 + 16.456.*TC - 0.0051176*TC.^2)/Mqtz; % quartz in LCO
granitic melt with 4 wt% water, 6.5 kbar
GPlag4_65 = ( -39514 + 46.227*TC)/Malb; %feldspar in LCO granitic melt with 4
wt% water, 6.5 kbar

%Mt Mica------------------------------
GqtzM4_63 = (-10336 +15.838 * TC - 0.0046192 * TC.^2)/Mqtz; % quartz in Mt.
Mica granitic melt with 4 wt% water, 6.3 kbar
GPlagM4_63 =  (-37423 + 34.086 * TC+0.0082939*TC.^2)/Malb; %feldspar in Mt
Mica granitic melt with 4 wt% water, 6.3 kbar

%End Mt Mica-------------------------



%GPlagB = (-1.2617e+08.*TKinv + 85759)/((Malb+Manth)/2);    %plagioclase in
basaltic melt (Gibb, 1974)

%GFsparLCODry = (92127 - 1.6857e+08 * TKinv +
6.3711e10*TKinv.^2)/((Malb+Manth)/2); %Feldspar in dry LCO 1020 -620 C
%GQtzLCODRY = (11287 - 1.9251e+07 * TKinv + 6.7408e+09 * TKinv.^2)/Mqtz;
%Quartz in dry LCO 1020 - 620 C



ending = length(TC);

GPlag5 = GPlagM4_63;

Gqtz5 = GqtzM4_63;

% **************set diffusion parameters************************
% choose which of the above set of Arrhenius parameters to use by
% changing the variables on the R.H.S. of the equations below:

%Dnot = DoAlB;  % Al in basalt
%Eact = EaAlB;  % Al in basalt
```

```
Dnot = Do; % This works well for hydrous granitic nucleation delay time
Eact = Ea-0.50*DeltaEa;  % This works well for hydrous granitic
%nucleation delay times

% granite calculation results
% The following data produce nucelation delat times that are far too long
%Dnot = 1.37e-4;%  Do for Si tracer diffusion in dry albite melt (Baker 1995)
%Eact = 337400; %  Ea for Si tracer diffusion in dry albite melt (Baker 1995


%HeteroCorr = 1; %correction for heterogeneous nucleation
     %!!!!!!!!!!!!!!!!!!!!!!!!Correction for Heterogeneous Nucleation
   % comment out for no correction
 % set for only 1 wetting angle for both crystals, 45 o
 Wtheta = 89*pi/180;  % covert wetting angle from degrees to radians
 HeteroCorr = (1/2 - 3/4*cos(Wtheta) + 1/4*(cos(Wtheta))^3)^(1/3) ; %Eqn 7.18
& 7.4 Gutzow & Schmelzer



MaxT=max(TC);
%***********start calculations through previously set T range***********
for i=1:ending

  D=Dnot*exp(-Eact/(R*TK(i)));


  %This is the place to insert a T-dependent sigma
  %sigma = sigmanot;
  %comment out the following line to remove effect of T on sigma
  %sigma = sigmanot -(TK(i)-273)*0.1e-3; % Fokin et al.(2006) Fig 15
  %sigma = sigmanot -8.5e-10*GPlag5(i); % Fokin et al. (2010) Fig. 7
  %sigma = sigmanot -7e-10*GPlag5(i);  % Fokin et al. (2010) Fig. 4

  % Calculation of Rc (critical radius) and sigma following Abyzov et al.
  % (2013)
  Rc=2*sigmanot/abs(GPlag5(i))- 2*delta;
  sigmaPlag = sigmanot/(1 + (2*delta)/Rc);
  Rc=2*sigmanot/abs(Gqtz5(i))- 2*delta;
  sigmaqtz = sigmanot/(1 + (2*delta)/Rc);

  %Hammer 2004 relationship between Delta T (undercooling) and sigma
  %DeltaT=MaxT-TC(i)
  %sigma = 0.019907+0.0003851*DeltaT;
  %  Hammer relationship does not work well--nucleation max too low and too
  %  high in temperature

  %***********Monika's values for testing 8 Sept 2019*******************:
wtH2O = 0.4;  % wt% water at the interface of nucleus and melt
sigmaHammer = -0.0176.*wtH2O+0.1121; % equation  H2O from Hammer 2004 --
surface free energy (J/m^2), good for 0 to 3 wt% water in melt
sigmaPlag = sigmaHammer;
sigmaqtz = sigmaHammer;
lambda = 0.26e-10; % diffusion jump distance (m)(silicon, Shanon (1976))
```

```
%Eact based upon water concentration fit to Baker (1992) for interfacial
water concentrations
Ea = 236554.097619; % J/mol 70 % SiO2 (Baker 1990)

DeltaEa = 36633; % J/mol %Slope of the line that relates Ea to water content

Eact=Ea-(wtH2O)*DeltaEa;


 % ***************end Monika's values for testing 8 Sept 2019*************

  %*****************************Calculating nucleation delay time
  %after Nascimento et al. (2011)
  TauNPlag(i) =
HeteroCorr^(1/3)*(80/3)*((h*sigmaPlag)/(lambda^4*GPlag5(i)^2))*exp(Eact/(R*TK
(i)));
  %comment out the following line when looking only at plag in basalt
  TauNQtz(i) = HeteroCorr^(1/3)*
(80/3)*((h*sigmaqtz)/(lambda^4*Gqtz5(i)^2))*exp(Eact/(R*TK(i))); % Do not use
for basalt


  %after Fokin et al. (2006)
  TauFPlag(i) = HeteroCorr^(1/3)*
(16*h)/pi*((sigmaPlag)/(lambda^4*GPlag5(i)^2))*exp(Eact/(R*TK(i)));
  %comment out the following line when looking only at plag in basalt
  TauFQtz(i)  =
HeteroCorr^(1/3)*(16*h)/pi*((sigmaqtz)/(lambda^4*Gqtz5(i)^2))*exp(Eact/(R*TK(
i))); %Do not use for basalt
  % Note that these Fokin et al. (2006) equations are very sensitive to:
  % Eact and lambda

  %************************************************************************

  % ****************Now calculate the nucleation rate*********************

  Io = 2*(1/(4/3*pi*lambda^3))*((kb*TK(i))/h)*
((lambda^2*sigmaPlag)/(kb*TK(i)))^0.5;
   % Io consistent with Fokin et al. (2006) J Non-Cryst Solids
   % Io varies from 3.24 x 1o^43 at low T to 4.24 x 10^43 at high T for
   % granite -- i.e., it is almost a constant

   % WPlag and WQtz are the free energies of formation of the critical
   % nuclei of each crystalline phase

  WPlag = (16*pi)/3 * (sigmaPlag^3)/(GPlag5(i))^2; %WPlag ~ 3 x 10^-15 J
  WQtz = (16*pi)/3 * (sigmaqtz^3)/(Gqtz5(i))^2;


  EactMolecule = Eact/Ao; %EactMolecule ~ 4 x 10^-19
  % Testing for similarity with estimates for metals in Markov p. 121
  % Markov gives for Silver crystalliation EactMolecule/kT ~ 3
  %EactMolecule/(kb*TK(i))  % my calculation yields ~ 25
  %testing if I change the value to 3
  %EactMolecule = 3*kb*TK(i)
```

```
 %Correcton for heterogeneous nucleation
 %WPlag = WPlag*HeteroCorr;
 %WQtz = WQtz*HeteroCorr;
  %*********************************************************% the factor
of ~10 doesn't make a difference

  SummPlag = WPlag+EactMolecule;
  SummQtz = WQtz+EactMolecule;

  %Fokin et al. (2006) JNCS -- gives high nucleation rates at low T,
  IstPlag(i) = Io*exp(-(SummPlag)/(kb*TK(i)));
  IstQtz(i) = Io*exp(-(SummQtz)/(kb*TK(i)));

  %Schmelzer (2010) JNCS Equation 7
 % IstPlag(i) = (sigmaPlag/(kb*TK(i)))^0.5*(D/lambda^4)*exp(-
WPlag/(kb*TK(i)));
  %IstQtz(i) = (sigmaqtz/(kb*TK(i)))^0.5*(D/lambda^4)*exp(-WQtz/(kb*TK(i)));

  %Schmelzer (2010) JNCS Equation 11 -- gives high nucleatio rates at low T
  %IstPlag(i) = (sigmaPlag/(kb*TK(i)))^0.5*((kb*TK(i))/(h*lambda^2))*exp(-
(WPlag+EactMolecule)/(kb*TK(i)));
  %IstQtz(i) = (sigmaqtz/(kb*TK(i)))^0.5*((kb*TK(i))/(h*lambda^2))*exp(-
(WQtz+EactMolecule)/(kb*TK(i)));


  TimeOverTau = 1.5; % time is 10x tau

  %Fokin et al. (2006)--integrated number of nuclei over time --see
  %TimeOverTau
  NvTauFPlag(i) =IstPlag(i).* (TimeOverTau.*TauFPlag(i)-(pi^2/6).*
TauFPlag(i));
  NvTauFQtz(i) = IstQtz(i) .* (TimeOverTau.*TauFQtz(i)-(pi^2/6).*
TauFQtz(i));

  %Markov book (2005)--integrated number of nuclei over time --see
  %TimeOverTau
    Summ = 0.0;
  for m=1:10000
      Summ = Summ + (-1)^m/m^2 * exp( -m^2*(TimeOverTau));
  end
  NvTauFPlag(i) =IstPlag(i).* TauFPlag(i)*(TimeOverTau + pi^2/6 - 2* Summ);
  NvTauFQtz(i) = IstQtz(i) .* TauFQtz(i)*(TimeOverTau + pi^2/6 - 2* Summ);

  % testing for relative nuclei to Ist at t=10x(Tau)
  %NvTauFPlag(i) = 1 * (10.*TauFPlag(i)-(pi^2/6) * TauFPlag(i));
  %NvTauFQtz(i) = 1 * (10.*TauFQtz(i)-(pi^2/6) * TauFQtz(i));

  Summ = 0.0;
  for m=1:10000

      Summ = Summ + (-1)^m * exp( -m^2*(TimeOverTau));
  end
  ITauFPlag(i) = IstPlag(i) * ( 1 + 2*Summ);
  ITauFQtz(i) = IstQtz(i) * ( 1 + 2*Summ);
```

```
%another estimate for tau based upon steady state nucleation rates
%tau_ss = 1/(J*Volume)
volume=0.001^3;    %Sample volume 0.001^3 = 1 mm^3
tau_ss_plag = 1./(volume*IstPlag./3600);  % convert and use hours
tau_ss_qtz = 1./(volume*IstQtz./3600);  % convert and use hours

  %***************End nucleation rate and density calculations***********
end

% ********Output Results************************
% convert from seconds to hours
% comment out the following lines with TauNQtz and TauFQtz for basalt
TauNPlag=TauNPlag/3600;
TauNQtz=TauNQtz/3600;
TauFPlag=TauFPlag/3600;
TauFQtz=TauFQtz/3600;

% for i=1:ending
%     fprintf('\n');
%     fprintf(' %4.0f,oC, Tau Plag Nascimento 2011 (h) %6.2f,    Tau Plag
Fokin et al. 2006 (h) %6.2f \n', TC(i),TauNPlag(i),TauFPlag(i));
%     % comment out the following line for plag in basalt
%     fprintf(' %4.0f,oC, Tau Qtz  Nascimento 2011 (h) %6.2f,    Tau Qtz
Fokin et al. 2006 (h) %6.2f\n', TC(i),TauNQtz(i),TauFQtz(i));
%
% end
%
% fprintf('Heterogeneous nucleation correction factor = %6.1e
\n',HeteroCorr);
%
% figure('Name','Nucleation Delay Time')

% comment out the following line for plag in basalt
% note you can choose TauFQtz or TauNQtz, the same is true for plag
plot(TauFQtz,TC,'b')
hold on
plot(TauFPlag,TC),'r')
hold on
legend('quartz','feldspar')

set(gca, 'XScale', 'log')
set(gca,'XLim',[1e-6,1e6])
xlabel('time (h)')
ylabel('Temperature (^oC)')
% plot(tau_ss_plag,TC,'+r')
% plot(tau_ss_qtz,TC,'go')


% figure('Name','Plag Affinity')
%
% set(gca, 'YScale', 'log')
% ylabel('Affinity (J/m^3)')
% xlabel('Temperature (^oC)')
% hold on
% plot(TC,(GPlag5))
%
```

```
% figure('Name','Nucleation Rate')
% set(gca, 'YScale', 'linear')
% ylabel('Nucleation rate (#/s m^3)')
% xlabel('Temperature (^oC)')
% hold on
% plot(TC,IstPlag)
% plot(TC,IstQtz)
%
% figure('Name','<tau>_SS')
% set(gca, 'YScale', 'linear')
% set(gca, 'XScale', 'log')
% set(gca,'XLim',[1e-6,1e6])
% ylabel('Temperature (^oC)')
% xlabel('Time (h)')
% hold on
% plot(tau_ss_plag,TC,'+r')
% plot(tau_ss_qtz,TC,'-')
%
%
%
% %Modify the following line to control what data are output to .csv file
% %Comment out following lines to suppress writing on .csv file
%
% TimeTC=[TauFQtz',TauFPlag',TC']; % Change variables to change stored data
% %Careful!  Change file location and name as appropriate!
% csvwrite('/users/maudebilodeau/Documents/00 √©cole/U2 research -
nucleation/int_water_0.75NucleationDelayFokinGraniteSiIonicSigmaMaude6_5kbar_
H2O_4_Granite_Qtz_Plag_time_TC9nov2019.csv',TimeTC);
%

Plag_TimeTC=[TauFPlag',TC']; % Change variables to change stored data
Qtz_TimeTC=[TauFQtz',TC'];
%Careful!  Change file location and name as appropriate!
csvwrite('/users/maudebilodeau/Documents/00 √©cole/ma√Ætrise/matlab
code/data_april2023/89deg_w_angle__intwater_0_Plag_tau_14april2023.csv',Plag_
TimeTC);
%csvwrite('/users/maudebilodeau/Documents/00 √©cole/ma√Ætrise/matlab
code/data_april2023/89deg_w_angle_intwater_0.4_Qtz_tau_april2023.csv',Qtz_Tim
eTC);


% %Use the following line to output results to screen
% %TT=table(TauFQtz',TauFPlag',TC')
% %T1 = table(TC',GPlag5')
```